The Company of Biologists

RESEARCH ARTICLE

Localized TPC1-mediated Ca^{2+} release from endolysosomes contributes to myoseptal junction development in zebrafish

Keira L. Rice, Sarah E. Webb and Andrew L. Miller*

ABSTRACT

In the trunk of developing zebrafish embryos, adjacent myotome blocks transmit contractile force via myoseptal junctions (MJs), which are dynamic structures that connect the actin cytoskeleton of skeletal muscle cells to extracellular matrix components via transmembrane protein complexes in the sarcolemma. Here, we report that the endolysosomal ion channel, two-pore channel type 1 (TPC1, encoded by *tpcn1*), generates highly localized non-propagating Ca^{2+} transients that play a distinct and required role in the capture and attachment of superficial slow skeletal muscle cells at MJs. Use of antisense morpholinos or CRISPR/Cas9 gene editing to disrupt *tpcn1* gene expression resulted in abnormal MJ phenotypes, including slow skeletal muscle cells detaching from or crossing the myosepta. We also report that TPC1-decorated endolysosomes are dynamically associated with MJs in a microtubule-dependent manner, and that attenuating *tpcn1* expression or TPC1 function disrupted endolysosomal trafficking and resulted in an abnormal distribution of β-dystroglycan (encoded by *dag1*; a key transmembrane component of the dystrophin-associated protein complex). Taken together, our data suggest that localized TPC1-generated Ca^{2+} signals facilitate essential endolysosomal trafficking and membrane contact events, which help form and maintain MJs following the onset of slow skeletal muscle cell contractile activity.

This article has an associated First Person interview with the first author of the paper.

KEY WORDS: Endolysosomes, Ca^{2+} signaling, Two-pore channel type 1, Myoseptal junctions, Slow skeletal muscle cells, Zebrafish

INTRODUCTION

In zebrafish embryos, many aspects of the development and differentiation of the trunk musculature are well documented (Devoto et al., 1996; Blagden et al., 1997; Cortés et al., 2003; Ono et al., 2015). Teleost skeletal muscles are organized as a series of somite-derived myotome blocks, which extend the length of the trunk (Fig. 1A; Fig. S1A). Each myotome block is separated by a vertical myoseptum, which is functionally homologous to mammalian tendons (Gembella and Vogel, 2002). The myoseptum contains a collagen fibril-rich extracellular matrix (ECM), to which the actin cytoskeleton of individual myofibers is attached via multi-protein

The Division of Life Science and Key State Laboratory for Molecular Neuroscience, The Hong Kong University of Science and Technology, Clear Water Bay, Hong Kong, The PRC.

*Author for correspondence (almiller@ust.hk)

K.L.R., 0000-0001-7403-261X; S.E.W., 0000-0002-0108-6606; A.L.M., 0000-0003-0237-317X

complexes forming myoseptal junctions (MJs; Charvet et al., 2011). The MJs are the site of force transmission at the onset of prehatching trunk coiling contractions (Saint-Amant and Drapeau, 1998) and during subsequent swimming behavior (Naganawa and Hirata, 2011). In each myotome block there are two main types of skeletal muscle cell, slow muscle cells (SMCs), the focus of this report, and fast muscle cells (FMCs; Fig. 1A; Fig. S1A–C) (Devoto et al., 1996). The SMCs arise from adaxial cells, which originate in a medial position adjacent to the notochord (Blagden et al., 1997), and these can be classified into two main types, superficial SMCs, and muscle pioneer cells (Fig. S1B). Both types of progenitor cell elongate in a rostral–caudal direction in each myotome block and migrate as mononucleate cells through the paraxial mesoderm (composed mainly of FMC precursors) until they reach the periphery of the trunk myotome (Devoto et al., 1996; Cortés et al., 2003; Stellabotte and Devoto, 2007; Ono et al., 2015). Following elongation, the medial surface of the muscle pioneer cells remains adjacent to the notochord, distinguishing them from the superficial SMC population. On reaching the myotome periphery, dynamic interactions occur between the terminal sarcolemma of each superficial SMC and the ECM in the vertical myoseptum, which results in a molecular coupling to prevent detachment of the superficial SMCs when contraction begins at ∼17 h post fertilization (hpf) (Henry et al., 2005; Charvet et al., 2011; Wood and Currie, 2017). The attachment of the superficial SMCs at the MJ involves component delivery and assembly of transmembrane protein complexes such as the dystrophin-associated protein complex (DAPC), which links the actin cytoskeleton in the SMCs to laminins in the myoseptal ECM via the large rod-shaped protein, dystrophin and the laminin receptor dystroglycan (Fig. S1D; Basset et al., 2003; Guyon et al., 2003).

It is recognized that zebrafish skeletal muscle differentiation is regulated by multiple signaling networks (Jackson and Ingham, 2013), some of which are better understood than others. Here, we investigated the regulatory role played by the ubiquitous second messenger, Ca^{2+} (Berridge et al., 2003). Distinct, highly reproducible patterns and frequencies of propagating pan-cellular Ca^{2+} transients have been reported to be required for early myofibrillogenesis in zebrafish SMCs (Brennan et al., 2005; Cheung et al., 2011; Kelu et al., 2015, 2017), but not for the migration or elongation of these cells (Brennan et al., 2005). This highly reproducible series of propagating Ca^{2+} transients are first generated between ∼17–20 hpf in both the cytoplasmic and nuclear domains of differentiating SMCs. These are suggested to be associated with excitation–transcription coupling and subsequent myofibrillar organization (Brennan et al., 2005; Cheung et al., 2011), and they coincide with early spontaneous coiled contraction movements of the embryonic trunk (Saint-Amant and Drapeau, 1998). A second phase of SMC-generated pan-cellular Ca^{2+} transients, which starts at ∼23 hpf, is restricted to the cytoplasmic domain and is proposed to be associated mainly with excitation–contraction coupling (Cheung et al., 2011). These later transients coincide with the initiation of the
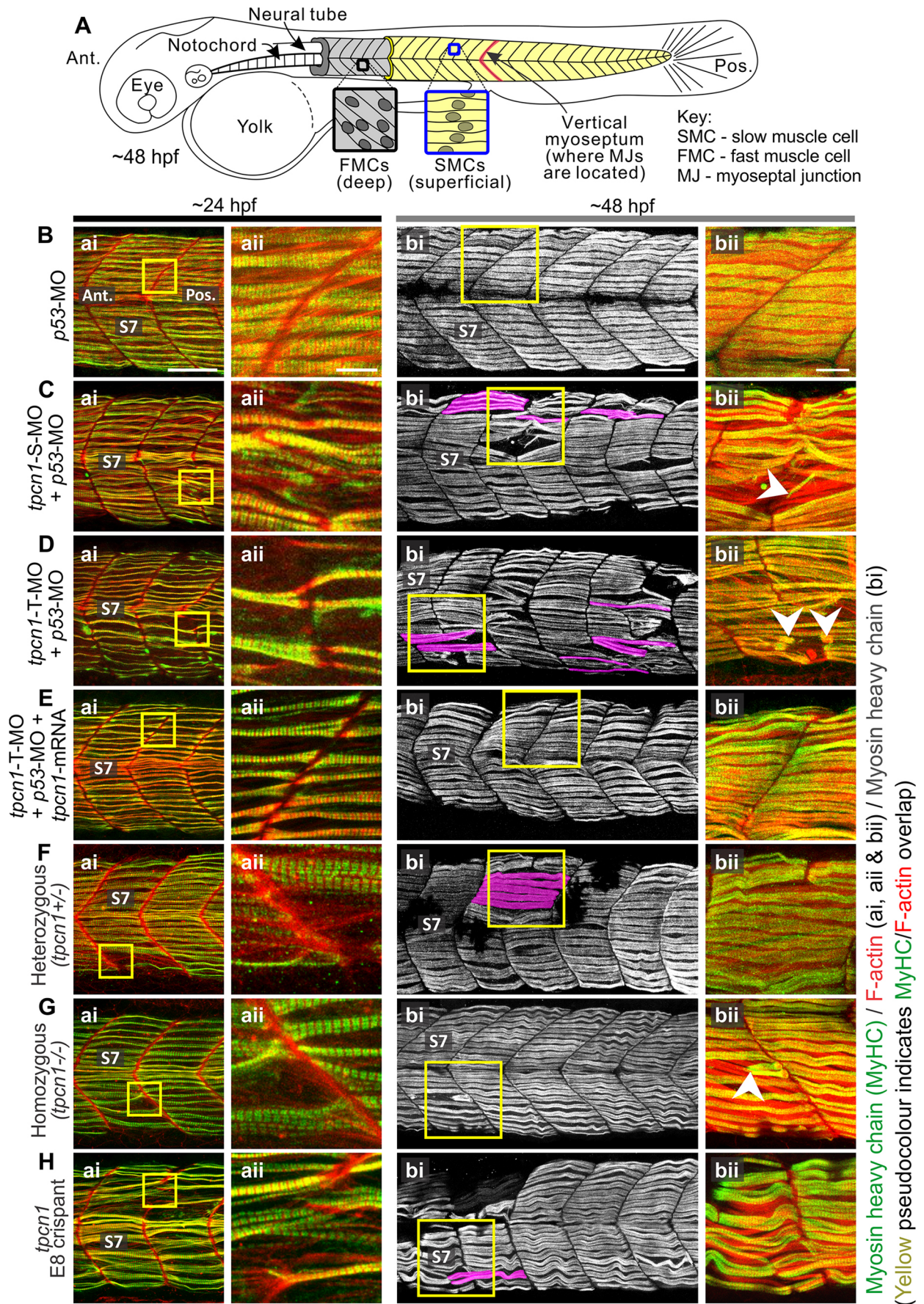
Fig. 1. See next page for legend.

Fig. 1. Arrangement of skeletal muscle in the zebrafish trunk at ∼24 hpf and effect of MO-based knockdown and CRISPR/Cas9 knockout of *tpcn1* on the organization of SMCs at ∼24 and ∼48 hpf. (A) Schematic showing the location of the slow and fast muscle cells as well as the vertical myoseptum in the zebrafish trunk. Ant., anterior; Pos. posterior. (B–E) Embryos were injected at the one- to four-cell stage with (B) *p53*-MO, (C) *tpcn1*-S-*MO* plus *p53*-MO, (D) *tpcn1*-T-MO plus *p53*-MO, or (E) *tpcn1*-T-MO plus *p53*-MO and *tpcn1*-mRNA rescue construct. (F–H) Representative (F) heterozygous and (G) homozygous *tpcn1* mutants, and (H) *tpcn1* E8 crispants. In B–H, embryos were fixed at ∼24 hpf (ai and aii panels) or ∼48 hpf (bi and bii panels) and then the myosin heavy chain (green in ai, aii, bii panels, grayscale in bi panels) and F-actin (red) were labeled. The regions bounded by yellow squares in the ai and bi panels are shown at higher magnification in the aii and bii panels, respectively. In Cbi, Dbi, Fbi and Hbi, myofibers that cross the somite boundaries are shown in magenta. In Cbii, Dbii and Gbii, detached SMCs are indicated by white arrowheads. S7, somite 7. Images are representative of 5–23 embryos. Scale bars: 50 μm (ai and bi panels), 20 μm (bii panels), 10 μm (aii panels).

evoked swimming behavior that begins at ∼26 hpf (Saint-Amant and Drapeau, 1998). The bulk of the Ca^{2+} generating these early myogenic transients is released mainly from the sarcoplasmic reticulum (SR) of SMCs via a combination of inositol (1,4,5)-trisphosphate receptors and ryanodine receptors (Brennan et al., 2005; Cheung et al., 2011). However, it has recently been reported that these Ca^{2+} signals are initiated via the action of two-pore channel (TPC) type 2 (TPC2, encoded by *tpcn2* in zebrafish) (Kelu et al., 2015, 2017), perhaps via a proposed triggering mechanism (Zhu et al., 2010a). Indeed, the knockdown or pharmacological inhibition of TPC2 completely eliminates both phases of the propagating Ca^{2+} transients in SMCs and results in a disruption of myofibrillogenesis and subsequent motility (Kelu et al., 2017).

TPCs are members of the voltage-gated ion channel superfamily (Calcraft et al., 2009; Zhu et al., 2010a; Galione, 2019). To date, three TPC isoforms (TPC1, TPC2 and TPC3) have been identified and these are localized on different components of the endolysosomal trafficking pathway. TPC1 (encoded by *tpcn1* in zebrafish) and TPC3 (encoded by *tpcn3* in zebrafish) are predominantly (but not exclusively) expressed on endosomes, whereas TPC2 is localized primarily on lysosomes (Calcraft et al., 2009). TPCs are described as being master regulators at the intersection of endolysosomal membrane trafficking (Marchant and Patel, 2015; Grimm et al., 2017; Vassileva et al., 2020). However, compared to TPC2-mediated Ca^{2+} signaling, less is known about the regulatory role played by TPC1 during skeletal muscle myogenesis. Addressing this question was the rationale for this work, which used zebrafish as a familiar and well-suited model system. It is known that heterotypic organelle interactions take place between endolysosomes and other membrane-bound organelles, including the endoplasmic reticulum (ER) (Kinnear et al., 2004; Kilpatrick et al., 2013), nucleus (Chaumet et al., 2015), and *trans* Golgi-network (Jung et al., 2012) as well as the plasma membrane itself (Klumperman and Raposo, 2014). In addition, homotypic and heterotypic interactions occur between endolysosomes, and these are suggested to be responsible for key processes associated with trafficking, the maintenance of cellular homeostasis, autophagy and the regulation of developmental events (Dowling et al., 2008; Lin et al., 2015; Grimm et al., 2017). Reports indicate that TPC-mediated Ca^{2+} signaling might play a significant role in regulating these various organellar membrane interactions (Zhu et al., 2010b; Kilpatrick et al., 2017; Davis et al., 2020). The importance of TPC activity in these events is clearly indicated via attenuation of their function, which results in a diverse range of disease phenotypes (Patel and Kilpatrick, 2018; Jin et al., 2020; Moccia et al., 2021).

As TPC-related isoform-specific roles have previously been reported from experiments using *Xenopus* oocytes and cultured mammalian cells (Lin-Moshier et al., 2014), we hypothesized that Ca^{2+} release from TPC1 might have independent and distinct developmental and/or regulatory functions from TPC2 during myogenesis in SMCs. Thus, here we used a combinatorial approach (by applying genetic, molecular, pharmacological, and various live- and fixed-imaging techniques in both intact embryos and cultured SMCs) to explore the role of TPC1-mediated Ca^{2+} signaling during SMC myogenesis at ∼24 hpf and ∼48 hpf. We report that unlike the pan-cellular Ca^{2+} transients triggered by TPC2, TPC1 generates localized non-propagating (LNP) Ca^{2+} transients that regulate essential endolysosomal trafficking and organellar membrane contact site activity at the sarcolemma–vertical myoseptal interface. These events appear to be essential for forming and then maintaining the MJs once the SMCs begin to contract, as well as for terminating the elongation of these cells, which prevents them from crossing the myoseptal boundaries. As attenuation of TPC1-mediated Ca^{2+} release results in phenotypes that resemble various dystroglycanopathies, we discuss how TPC1 might represent a possible target for therapeutic intervention.

RESULTS

Generating knockdown and knockout models of *tpcn1* in zebrafish

To investigate the potential role of TPC1 in SMC attachment and stabilization at the MJ (Fig. S1), we attenuated the expression of *tpcn1* via the use of morpholino oligonucleotides (MOs; Figs S2, S3) and by generating a mutant line via CRISPR/Cas9 mutagenesis (Fig. S4). Splice- and translation-blocking *tpcn1* MOs (*tpcn1*-S-MO and *tpcn1*-T-MO, respectively) were designed, and their efficacy characterized by reverse transcription polymerase chain reaction (RT-PCR) analyses of *tpcn1* transcripts and the attenuation of TPC1–EGFP fluorescence, respectively (Figs S2,S3). Our MO results were compared with *p53* (also known as *tp53*)- and standard control (SC) MOs, and rescue experiments were performed for the *tpcn1*-T-MO using a *tpcn1* mRNA construct (*tpcn1*-mRNA). The latter indicated the specificity of MO-based knockdown.

We characterized two gene loss-of-function models by generating a stable *tpcn1* mutant knockout line carrying a 16 bp insertion in exon 5 (named *tpcn1^{dhkz101}* in accordance with the ZFIN zebrafish nomenclature guidelines; http://zfin.org), and a first generation (F_0) *tpcn1* mosaic mutant (hereafter referred to as a *tpcn1* 'E8 crispant') using a single guide RNA targeting exon 8 (Fig. S4). The knockdown of *tpcn1* transcripts in homozygous *tpcn1* mutants and the effective generation of indels in *tpcn1* were validated by quantitative RT-PCR (qRT-PCR), Sanger sequencing and high-resolution melting analysis (HRMA; Fig. S4).

Effect of MO-based knockdown and CRISPR/Cas9 knockout of *tpcn1* on SMC organization

We investigated whether *tpcn1* knockdown or knockout might affect any gross aspects of SMC development. Fig. 1B–H shows the gross morphology of [and the localization of myosin heavy chain (MyHC) and F-actin in] the skeletal musculature of *tpcn1* morphants, mutants and E8 crispants at ∼24 hpf (in somites 7 and 8) and ∼48 hpf (in somites 7 to 11). [Note, the specific isotypes of myosin heavy chain recognized by the antibody F59, as used here, in zebrafish are unknown; however, this antibody is widely used to label SMCs in early embryos (Devoto et al., 1996; Kelu et al., 2015).] Quantification of the morphological changes observed at these times is shown in Fig. 2.
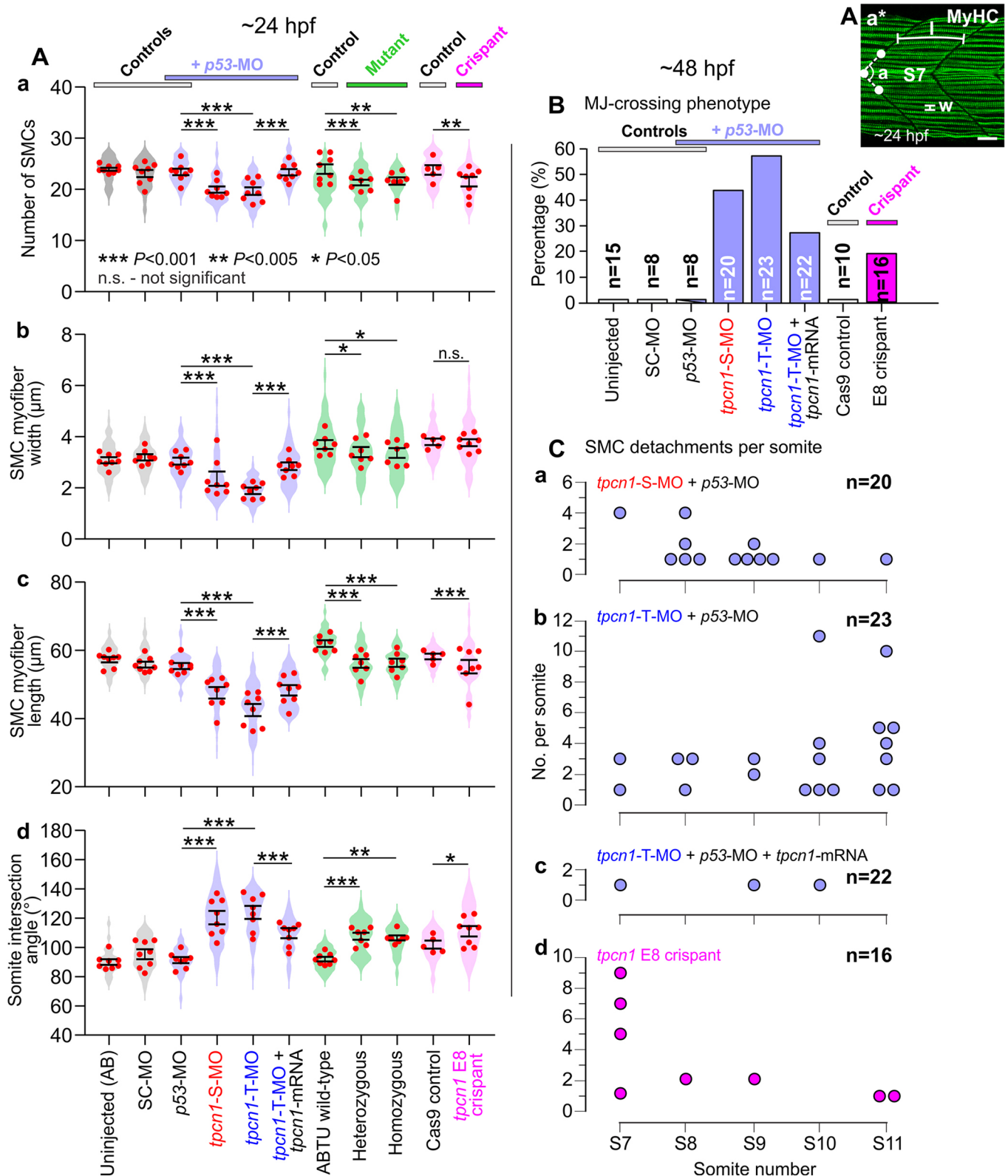
Fig. 2. Quantification of the effect of MO-based knockdown and CRISPR/Cas9 knockout of *tpcn1* on the organization of SMCs at ∼24 and ∼48 hpf. (A) Violin plots (with mean±s.e.m.) onto which are superimposed individual data points showing the (Aa) number of SMCs, (Ab) SMC myofiber width, (Ac) SMC myofiber length and (Ad) somite intersection angle in embryos at ∼24 hpf treated as described in Fig. 1. *n*=5–23. Panel Aa* (top right) shows a representative image of somite 7 (S7) in an uninjected AB wild-type embryo at ∼24 hpf. Myosin heavy chain is labeled in green, and the SMC myofiber length (l) and width (w), as well as the somite intersection angle (a), are indicated. Scale bar: 20 μm. (B) Bar chart indicating the percentage of embryos in each treatment group displaying myofibers that crossed the MJ boundary at ∼48 hpf. (C) Dot plots illustrating the number of SMC detachments from MJs in somites 7–11 at ∼48 hpf in embryos injected with (Ca) *tpcn1*-S-MO, (Cb) *tpcn1*-T-MO or (Cc) *tpcn1*-T-MO plus *tpcn1* mRNA (all plus *p53*-MO), and in (Cd) *tpcn1* E8 crispants. *P<0.05; **P<0.005; ***P<0.001; ns, not significant (one-way ANOVA and Fisher's LSD test).
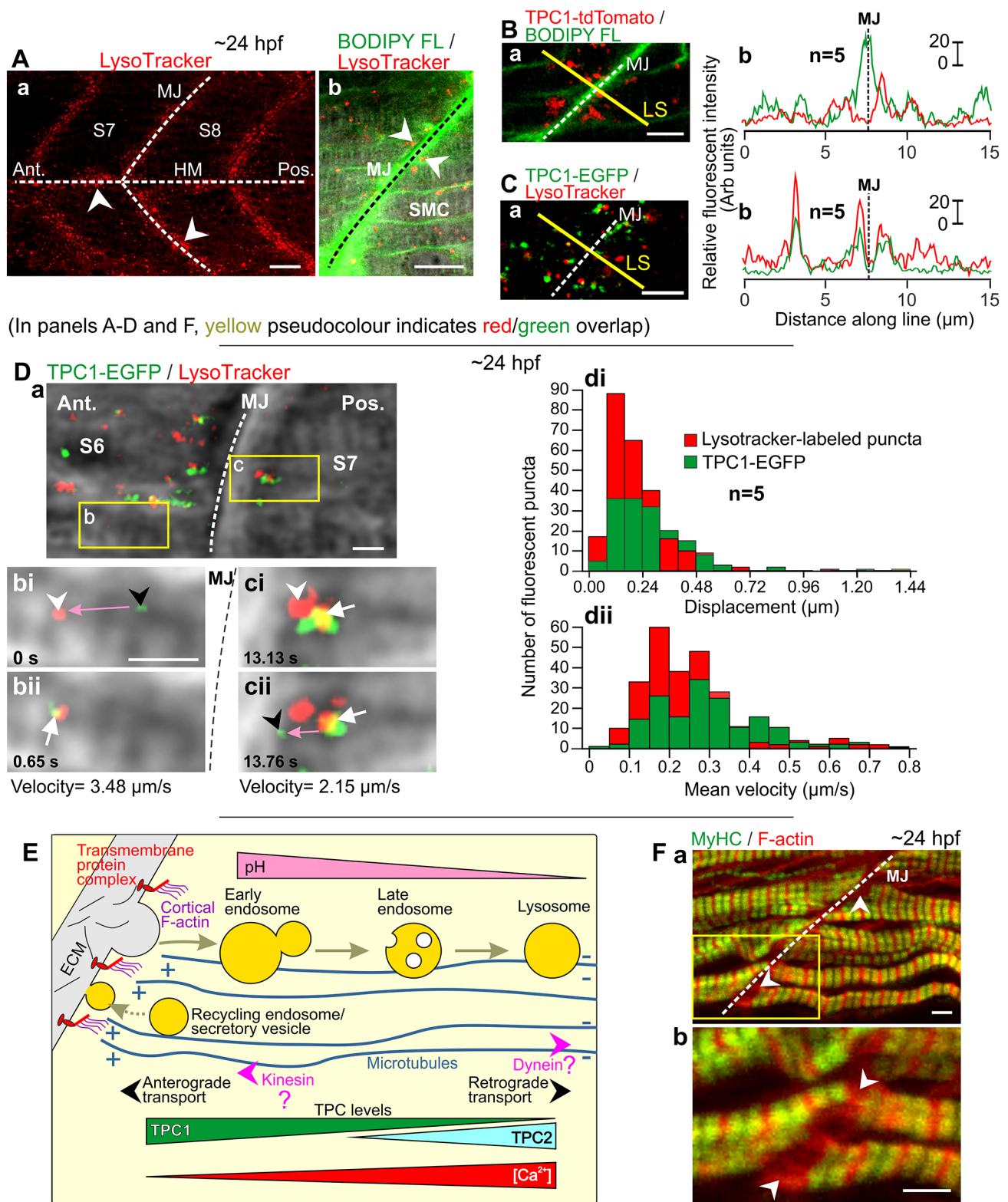
Fig. 3. See next page for legend.

At ~24 hpf, the *tpcn1* morphants exhibited a significant decrease in the number of SMCs and in the SMC myofiber width and length when compared with the various controls (untreated, SC-MO or *p53*-MO alone; Figs 1Bai,Cai,Dai and 2Aa–Ac). The morphants also exhibited more U-shaped somites instead of the usual chevron-shaped somites seen in the controls (compare Fig. 1Cai and Dai with Fig. 1Bai, and see Fig. 2Ad). The somite shape was quantified by measuring the somite intersection angle. This and the other dimensions measured are shown in Fig. 2Aa*. The abnormalities observed in the *tpcn1*-T-MO (plus *p53*-MO) group were partially

Fig. 3. Visualization of acidic organelles and TPC1 fusion proteins in SMCs. (Aa) Low magnification lateral view of somite 7 and 8 (S7 and S8, respectively) in AB wild-type embryos stained with LysoTracker (red) to label the acidic organelles (white arrowheads), adjacent to the horizontal myoseptum (dashed line HM) and myoseptal junctions (dashed line MJ). (Ab) Higher magnification view of LysoTracker fluorescence merged with the corresponding BODIPY FL (green) fluorescence and bright-field images to show acidic organelles at the ends of SMCs adjacent to the MJ (white arrowheads; MJ is marked with a dashed line). Images are representative of six embryos. (B,C) Representative confocal images of the MJ (dashed line) in AB wild-type embryos either (Ba) injected with *tpcn1–tdTomato* mRNA (red) and stained with BODIPY FL (green) or (Ca) injected with *tpcn1–EGFP* mRNA (green) and stained with LysoTracker (red). The yellow lines indicate line scans (LS) across the MJ. (Bb,Cb) Graphs indicating the relative fluorescence intensity for the red and green fluorescence signals along the line scans shown in Ba and Ca, respectively. Arb units, arbitrary units. (Da–Dcii) Representative confocal images of the MJ (dashed line in Da) between somite 6 and 7 (S6 and S7, respectively) of an intact AB wild-type zebrafish embryo at ~24 hpf injected with *tpcn1–EGFP* mRNA and stained with LysoTracker. The regions bounded by the yellow rectangles in Da are shown at higher magnification in Dbi–Dcii. These show (Dbi,Dbii) a TPC1-decorated vesicle (black arrowhead) moving in a retrograde direction (pink arrow) from the sarcolemma of the MJ to an acidic organelle (white arrowhead), and (Dci,Dcii) a TPC1-decorated vesicle (black arrowhead) moving in an anterograde direction (pink arrow) from a cluster of organelles (white arrow) labeled by TPC1–EGFP and LysoTracker (white arrowhead) towards the sarcolemma of the MJ. The merged TPC1–EGFP and LysoTracker fluorescence is yellow (white arrows in Dbii–Dcii). (Ddi,Ddii) Histograms showing the (Ddi) displacement and (Ddii) mean velocity of the TPC1–EGFP- and LysoTracker-labeled puncta tracked in Da. (E) Schematic illustration showing an overview of the reported differences in pH, localization of TPC1 and TPC2, and luminal Ca^{2+} concentration in the different endolysosomal components at the MJ (modified from Morgan and Galione, 2014). (F) Fluorescence images of an AB wild-type embryo showing that cortical actin (white arrowheads; F-actin is shown in red) does not overlap with sarcomeric myosin heavy chain (MyHC; green) at the MJ (dashed line). The region bounded by the yellow rectangle in Fa is shown at higher magnification in Fb. Images are representative of eight embryos. Ant., anterior; Pos., posterior. Scale bars: 20 µm (Aa), 10 µm (Ab), 5 µm (Ba,Ca), 2 µm (D,F).

rescued when embryos were co-injected with *tpcn1*-T-MO (plus *p53*-MO) and *tpcn1*-mRNA, such that the SMC myofiber length and width, and somite intersection angle were all partially restored (Figs 1Eai,Eaii and 2A). Similarly, injection of *tpcn1*-T-MO (plus *p53*-MO) also significantly inhibited the spontaneous coiling frequency of embryos between ~17.5 hpf and ~23.5 hpf, when compared with the *p53*-MO controls, whereas co-injection of *tpcn1*-T-MO (plus *p53*-MO) and *tpcn1*-mRNA partially rescued the inhibitory effect of the *tpcn1*-T-MO (Fig. S5).

At ~48 hpf, the *tpcn1* morphants exhibited more pronounced abnormalities at the MJ. For example, SMC boundary crossings (in magenta in Fig. 1Cbi,Dbi and quantified in Fig. 2B) were observed in ~40–52% of the morphants. SMC detachment from the MJ was also observed in the morphants (Figs 1Cbii,Dbii and 2C). This is despite the somite boundaries forming normally in the *tpcn1* morphants, as shown in the representative examples at ~17 hpf (Fig. S6A). At ~48 hpf, in somites 7–11, SMC detachment ranged from 1 to 11 detachments per somite (Fig. 2C), occurring at approximately equivalent frequencies from the posterior and anterior ends, and in the dorsal and ventral regions of the somite block (Fig. S6B). Co-injection of *tpcn1*-T-MO (plus *p53*-MO) and *tpcn1*-mRNA also partially rescued embryos at ~48 hpf, as a lower incidence of myotome boundary crossings and SMC detachments from the MJ were observed (Fig. 2B,C).

In the heterozygous and homozygous *tpcn1* mutant embryos, there was some recapitulation of the MO-induced phenotypes at ~24 hpf, such that there was a decrease in the number of SMCs, and

in the SMC myofiber length and width, as well as an increase in the somite intersection angle (Figs 1Fai,Faii,Gai,Gaii and 2A–C). However, the number of embryos displaying boundary crossings or SMC detachments at ~48 hpf was considerably lower, such that only 1 of 14 *tpcn1*$^{+/-}$ embryos produced an SMC myotome boundary-crossing phenotype and only 2 of 15 *tpcn1*$^{-/-}$ embryos showed SMC detachments (Fig. 1Fbi,Gbi). The function of *tpcn1* was also investigated in F_0 *tpcn1* E8 crispants (Fig. 1H). At ~24 hpf, there was a decrease in the number of SMCs, and in the SMC myofiber length (but not width), as well as an increase in the somite intersection angle (Fig. 2A). In addition, at ~48 hpf, ~19% of the *tpcn1* E8 crispants exhibited SMC myotome boundary crossing defects (Fig. 2B), and ~38% exhibited between 1 and 9 SMC detachments per somite in somites 7–11 (Fig. 2Cd).

Localization of acidic organelles at the MJ and sub-organellar distribution of TPC1 in intact embryos

Fig. 3 shows the localization of acidic organelles (including endolysosomes) in the trunk musculature of intact embryos stained with LysoTracker Red (referred to hereafter as LysoTracker) at ~24 hpf. Distinct accumulations of LysoTracker-labeled puncta were shown to be localized adjacent to the MJ (Fig. 3Aa). Co-labeling embryos with LysoTracker and BODIPY FL (to reveal the SMC sarcolemma) showed that LysoTracker-labeled puncta were localized at the ends of SMCs adjacent to the MJ (Fig. 3Ab). When embryos were injected with *tpcn1–tdTomato* mRNA and then labeled with BODIPY FL, TPC1-decorated puncta were observed to be closely associated with the MJ (Fig. 3Ba,Bb). In addition, when embryos were injected with *tpcn1–EGFP* mRNA and then labeled with LysoTracker, some LysoTracker-labeled puncta also exhibited TPC1–EGFP fluorescence, as seen by the yellow labeling (Fig. 3Ca,Cb).

TPC1–EGFP-expressing embryos labeled with LysoTracker were also used to investigate the dynamics of the TPC1-decorated vesicles in the vicinity of the MJ (Fig. 3D; Movie 1). TPC1–EGFP and LysoTracker-labeled puncta were tracked for 2 min using confocal microscopy (Fig. 3Da–Dcii). The TPC1–EGFP-labeled puncta were shown to move in both anterograde and retrograde directions, to and from the sarcolemma at the MJ. Although most of the puncta traveled distances of 0–0.72 µm, a small proportion of the TPC1–EGFP puncta traveled up to ~1.44 µm within this time-lapse series (Fig. 3Ddi). In addition, most of the puncta traveled at velocities of 0–0.8 µm/s (Fig. 3Ddii) although some moved more quickly, at velocities greater than 3.0 µm/s (Fig. 3Db,Dc). For example, as shown in Fig. 3Dbi and Dbii, a TPC1-decorated vesicle (black arrowhead) traveled in a retrograde direction at ~3.48 µm/s to an acidic organelle (white arrowhead), at which time an overlap in their fluorescence (white arrow) was observed. Later in this time-lapse series, another TPC1–EGFP-bearing vesicle was observed 'pinching off' from a cluster of TPC1–EGFP- and LysoTracker-positive organelles and moving in an anterograde direction at ~2.15 µm/s toward the MJ (Fig. 3Dci,Dcii). The schematic in Fig. 3E summarizes the reported differences in pH, localization of TPC1 (and TPC2) and luminal Ca^{2+} concentration in the different components of the endolysosomal pathway relative to the MJ, as well as the distribution of cortical F-actin, polarity of microtubules and direction of travel of microtubule motors [image modified with permission from John Wiley and Sons (Morgan and Galione, 2014)]. Fig. 3F shows the localization of cortical F-actin (white arrowheads) but not sarcomeric MyHC in the vicinity of the MJ.
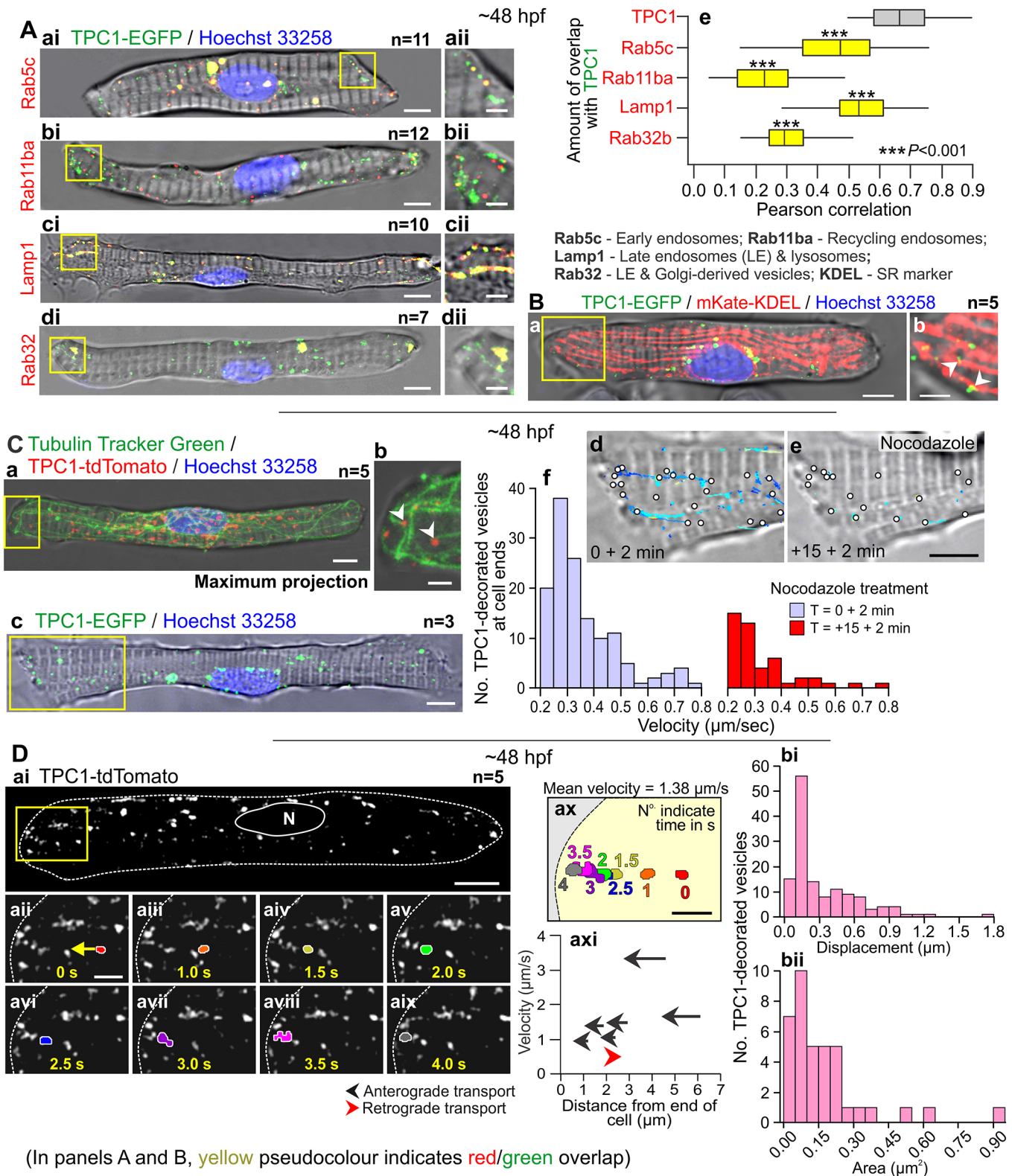
(In panels A and B, yellow pseudocolour indicates red/green overlap)

Fig. 4. See next page for legend.

Distribution of TPC1-decorated vesicles in cultured SMCs

To identify which members of the endolysosomal system were decorated with TPC1 in SMCs, embryos were co-injected at the one-cell stage with *tpcn1–EGFP* mRNA and a plasmid encoding mKate2-tagged Rab5c, Rab11ba, Lamp1 (also known as Lamp1b) or Rab32b

(Fig. 4Aai–Adii; Hall et al., 2020). Rab proteins are known to regulate key steps during membrane trafficking, including the formation, transport and fusion of vesicles (Hall et al., 2020). In addition, different Rabs (along with Lamp1) are expressed by (and can therefore be used to identify) specific components of the

Fig. 4. Distribution of TPC1 and dynamics of TPC1-decorated vesicles in cultured SMCs. (A) Representative confocal images of SMCs isolated from ~48 hpf embryos that had been injected with *tpcn1–EGFP* mRNA (green) and a plasmid encoding mKate2-tagged with (Aai) Rab5c, (Abi) Rab11ba, (Aci) Lamp1 or (Adi) Rab32 (all shown in red). Colocalization of the two fluorescent markers is shown in yellow. The regions bounded by the yellow squares in Aai, Abi,Aci,Adi are shown at higher magnification in the images on the right. (Ae) Box plot showing the Pearson correlation analysis of TPC1 colocalization with Rab5c, Rab11ba, Lamp1 or Rab32. Colocalization with tdTomato–TPC1–EGFP is shown as a positive control (*n*=8). Boxes indicate the interquartile range, whiskers show the minimum and maximum values, and the mean is marked with a line. ***$P<0.001$ (one-way ANOVA and Fisher's LSD test). (B) Confocal image of an SMC isolated from a ~48 hpf embryo that had been injected with *tpcn1–EGFP* mRNA (green) and a plasmid encoding the SR marker mKate2–KDEL (red). Colocalization of the two is shown in yellow. The region bounded by the yellow square in Ba is shown at higher magnification in Bb. White arrowheads indicate TPC1–EGFP puncta that are closely associated with the SR. (Ca) Representative confocal image of an SMC isolated from a ~48 hpf embryo that had been injected with *tpcn1–tdTomato* mRNA (red) and then incubated with Tubulin Tracker Green (green) to label TPC1 and microtubules, respectively. The region bounded by the yellow rectangle is shown at higher magnification in Cb, where the white arrowheads indicate TPC1–tdTomato puncta that are closely associated with the microtubules. (Cc) Representative confocal image of an SMC isolated from a ~48 hpf embryo injected with *tpcn1–EGFP* mRNA (green). The region bounded by the yellow rectangle is shown at higher magnification in Cd and Ce. These images display a tracking analysis overlay (lines) to show the displacement of TPC1–EGFP puncta (measured over a period of 2 min), just before (Cd) and 15 min after (Ce) treatment with 1 μM nocodazole. Circles indicate the end of tracks. (Cf) Histograms showing the velocity of TPC1-decorated vesicles before (purple) and after (red) treatment with nocodazole. The nuclei of the cells in A–C were labeled with Hoechst 33258 (blue). (Dai–Daix) Representative super-resolution images of an SMC isolated from an ~48 hpf embryo that had been injected with *tpcn1–tdTomato* mRNA. The region bounded by the yellow rectangle in Dai is shown at higher magnification in Daii–Daix; these are frames from a time-series that show a TPC1-decorated vesicle (traced and colored in each panel) moving in an anterograde direction (arrow) to the presumptive MJ. The SMC is outlined with a dashed line, and the nucleus (N) is marked. (Dax) Schematic summarizing the morphology and motility of the selected TPC1-decorated vesicle shown in Dai–Daix. Numbers indicate time in seconds. (Daxi) Graph displaying the velocity of the TPC1-decorated vesicle shown in Dai–Daix at different distances from the end of the cell, with anterograde movement shown in black and retrograde movement shown in red. (Db) Histograms showing the (Dbi) displacement and (Dbii) area of TPC1-decorated vesicles in the region bounded by the yellow box in Dai within the 25 s time series. Scale bars: 5 μm (Aai,Abi,Aci,Adi,Ba,Ca,Cc–Ce, Dai), 2 μm (Aaii,Abii,Acii,Adii,Bb,Cb,Daii–Dax).

endolysosomal system. For example, Rab5c is present on (and can be used to help identify) early endosomes, Rab11ba is present on recycling endosomes, Rab32b is present on late endosomes and Golgi-derived vesicles, and Lamp1 is present on lysosomes and late endosomes (Hall et al., 2020). Some embryos were co-injected with *tpcn1–EGFP* and *tpcn1–tdTomato* mRNAs as positive controls. Primary cultured cells were prepared at ~48 hpf, and the colocalization of TPC1–EGFP with these endolysosomal markers (or with TPC1–tdTomato) at the MJ of SMCs was determined. SMC primary cultures were used for several experiments because cells grown in culture have a better fluorescence signal-to-noise ratio than intact embryos. We showed that Lamp1 and Rab5c were the markers that correlated most strongly with TPC1 distribution at the end of cells, whereas Rab11 and Rab32 overlapped with TPC1 fluorescence to a lesser extent (Fig. 4Ae). By co-injecting embryos with *tpcn1–EGFP* mRNA and *mKate2–KDEL* DNA (as a marker of the SR) prior to primary cell culture, we showed that TPC1-decorated organelles were also closely associated with the SR throughout cultured SMCs (Fig. 4Ba), including the end regions that would have formed MJs in intact embryos (white arrowheads, Fig. 4Bb).

We also showed close associations between TPC1-decorated organelles and microtubules (Fig. 4C). Embryos were injected at the one-cell stage with *tpcn1–tdTomato* mRNA, and then the primary cultured SMCs were incubated with Tubulin Tracker Green. The localization of TPC1 puncta in relation to the distribution of microtubules is shown in a representative SMC (Fig. 4Ca,Cb). Treatment of TPC1–EGFP-expressing SMCs with nocodazole, which disrupts the polymerization of microtubules, led to a reduction in the velocity of the TPC1 puncta at the cell end (Fig. 4Cc–Cf).

Imaging SMCs expressing TPC1–tdTomato at super resolution allowed us to resolve the pleiotropic morphology of the dynamic TPC1-decorated endolysosomes (Fig. 4Da; Movie 2). These endolysosomes moved displacement distances of up to ~1.8 μm to and from the cell ends (Fig. 4Dbi) and exhibited a range of areas up to ~0.95 μm^2, although most were less than ~0.2 μm^2 (Fig. 4Dbii). In the example shown (Fig. 4Da), endolysosomes appear as small, large or ramified puncta. The time series in Fig. 4Daii–Daix shows a small endolysosome traveling in an anterograde direction toward the end of the cell; as this endolysosome moved, it became larger. Over the 4 s duration of the time series, the vesicle traveled with a mean velocity of ~1.38 μm/s (Fig. 4Dax); however, the velocity decreased as the vesicle approached the end of the cell (Fig. 4Daxi).

Attenuating *tpcn1* expression affects acidic organelle distribution at the MJ in intact embryos

We investigated the effect of *tpcn1* knockdown on the distribution and morphology of endolysosomes at the MJ in intact ~24 hpf embryos by visualizing LysoTracker fluorescence (Fig. 5). In embryos injected with *tpcn1*-S-MO or *tpcn1*-T-MO (both plus *p53*-MO; Fig. 5Ca,Da), and in *tpcn1*$^{-/-}$ mutant embryos (Fig. 5Ga), the normal distribution and size of LysoTracker-stained puncta were compromised when compared with those in control (untreated, *p53*-MO-injected or wild-type ABTU strain) embryos (Fig. 5Aa,Ba,Fa). Line-scan analyses of LysoTracker fluorescence across the MJ (yellow lines in Fig. 5Aa–Ga) showed that in the controls, most of the LysoTracker-labeled puncta resided within ~10 μm on either side of the MJ (Fig. 5Ab,Bb,Fb). In contrast, in the *tpcn1* morphants and mutants, the puncta were far more diffusely distributed (Fig. 5Cb,Db,Gb) and considerably larger (see yellow arrowheads in Fig. 5Ca,Da,Ga). However, a similar distribution and size of puncta as the controls was observed when *tpcn1*-T-MO plus *p53*-MO embryos were co-injected with the rescue *tpcn1*-mRNA (Fig. 5Ea,Eb). We quantified the distribution of the puncta by calculating the ratio of the number of puncta concentrated at the MJ compared to those in the total imaged area (as shown in Fig. 5Hai). The data indicate that in the *tpcn1*-T-MO-injected embryos the ratio was significantly reduced when compared with the *p53*-MO controls, but that these effects were reversed by the injection of the rescue mRNA (Fig. 5Haii). We also quantified the area of individual MJ-associated puncta (Fig. 5Hb) and showed that MO-mediated knockdown of *tpcn1* led to these puncta being significantly larger, and co-injection with *tpcn1*-mRNA resulted in them resembling the puncta in the controls. In addition, the MJ-associated puncta were significantly larger in the *tpcn1*$^{-/-}$ mutants compared with those in the wild-type ABTU controls.

Distribution of β-dystroglycan is disrupted in *tpcn1* morphants and E8 crispants or following pharmacological inhibition of TPC activity in intact embryos

Fig. 6 shows the localization of β-dystroglycan (encoded by *dag1*) at the MJ in intact *tpcn1* morphants, E8 crispants or following
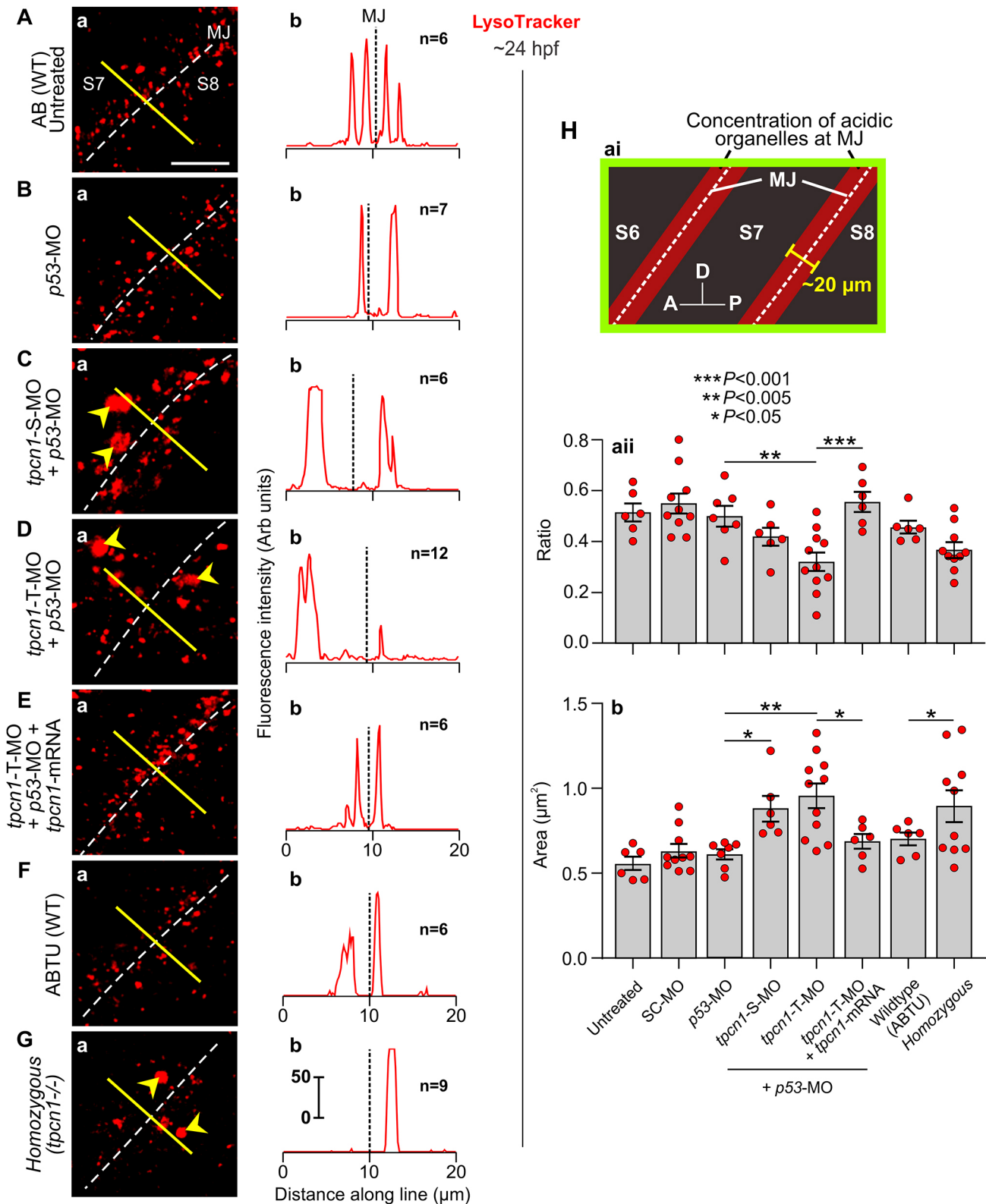
Fig. 5. See next page for legend.

treatment with the vacuolar proton pump (V-H⁺-ATPase) inhibitor bafilomycin A1 at ~24 hpf. The images in Fig. 6A–I are projected confocal stacks showing lateral views of somites 8 and 9, and the plots in Fig. 6A–I show the changes in fluorescence intensity along line-scans taken in the dorsal, midline and ventral regions of these

somites, as indicated by the yellow lines in Fig. 6Aa. The results indicate that β-dystroglycan was still partially localized in the dorsal, midline and ventral regions of MJs of the *tpcn1* morphants but, compared with the untreated and *p53*-MO controls, the relative level of MJ localization was reduced (compare Fig. 6C,D with

Fig. 5. Effect of attenuating *tpcn1* expression on the distribution of endolysosomes at the MJ in intact embryos. (A–E) AB strain wild-type (WT) embryos were (A) untreated, or (B–E) injected with (B) *p53*-MO, (C) *tpcn1*-S-MO plus *p53*-MO, (D) *tpcn1*-T-MO plus *p53*-MO, or (E) *tpcn1*-T-MO plus *p53*-MO and *tpcn1* mRNA. These embryos, as well as (F) ABTU strain WT and (G) *tpcn1*^{−/−} mutant embryos, were stained with LysoTracker. Representative confocal images showing lateral views in the dorsal region of somite (S) 7 and 8 are shown on the left. The yellow lines indicate the location of line scans across the MJ (dashed line). In panels Ca, Da and Ga, the yellow arrowheads indicate large LysoTracker-labeled puncta. Scale bar: 10 μm. Line graphs on the right show the relative fluorescence intensity of LysoTracker adjacent to the MJ for each of the confocal images (Arb units, arbitrary units). (H) Quantification of the puncta shown in A–G. (Hai) Schematic depicting a portion of the dorsal region of S6–S8, the concentration of acidic organelles (red) adjacent to the MJ (dashed line), and the region of interest (green rectangle) used to calculate the ratio values shown in Haii. The distribution ratio was defined as the ratio of the number of LysoTracker-stained puncta located in 10 μm-wide areas on either side of the MJ (bracket), compared with those in the entire imaged region. A, anterior; D, dorsal; P, posterior. (Haii,Hb) Bar charts (mean±s.e.m.) plus individual data points showing the (Haii) distribution ratio and (Hb) area of LysoTracker-stained puncta adjacent to the MJ in the indicated strains and treatments. The data were compared using one-way ANOVA and Fisher's LSD test.

Fig. 6A,B). However, when *tpcn1*-T-MO (plus *p53*-MO) was co-injected with the rescue *tpcn1*-mRNA, the level of β-dystroglycan localization more closely resembled that of the controls (compare Fig. 6E with Fig. 6A,B). The *tpcn1* E8 crispants and bafilomycin A1-treated embryos also exhibited a disrupted localization of β-dystroglycan at the MJs when compared with the Cas9 and DMSO vehicle controls, respectively (Fig. 6F–I). The number of puncta within a region of interest placed in the medial region of somite 8 was quantified in the morphants, E8 crispants and drug-treated embryos (Fig. 6Ja,Jb). Our data shows that the *tpcn1* morphants, E8 crispants and bafilomycin A1-treated embryos all exhibited a significant increase in the percentage area of β-dystroglycan-labeled puncta in a mid-somite region of interest when compared with their respective controls. However, when *tpcn1*-T-MO (plus *p53*-MO) was co-injected with the rescue *tpcn1*-mRNA, the percentage area was significantly lower than when *tpcn1*-T-MO (plus *p53*-MO) was injected alone (Fig. 6Jc).

Ca²⁺ signals generated in the trunk musculature of *tpcn1* morphants detected via aequorin-based luminescence

We investigated whether TPC1 might play some role in generating the pan-cellular Ca²⁺ signals that occur during early zebrafish development. Therefore, we assessed the effect of MO-mediated *tpcn1* knockdown on the three sequential SMC-generated Ca²⁺ signaling phases: signaling period 1 (SP1); quiet period (QP); and signaling period 2 (SP2; Cheung et al., 2011). We used transgenic *Tg(α-actin:aeq)* zebrafish embryos, which express apoaequorin (the protein component of the bioluminescent Ca²⁺ reporter aequorin) specifically in the skeletal muscle cells. Active aequorin was then reconstituted by incubating the embryos in a solution containing the apoaequorin cofactor, coelenterazine (Shimomura, 1997; Cheung et al., 2011). In these experiments, *Tg(α-actin:aeq)* embryos were injected at the one- to four-cell stage with *p53*-MO alone, or with *p53*-MO and either *tpcn1*-T-MO or *tpcn1*-S-MO. As shown in Fig. 7, when *tpcn1* expression was knocked down, distinct patterns of SP1, QP and SP2 were still observed, although there was a delay (∼60–90 min) in the start of SP1 (compare the signal start times in Fig. 7Ba and Ca with Fig. 7Aa). However, when the data were adjusted for the start of the SP1, *tpcn1* knockdown had no significant effect on the pattern or frequency of the pan-cellular Ca²⁺ signals when compared with the *p53*-MO controls (Fig. 7Ab,Bb,Cb).

Visualization of LNP TPC1-generated Ca²⁺ transients using TPC1–G-GECO in primary cultured SMCs

We investigated TPC1-mediated Ca²⁺ release by fusing TPC1 in-frame with a low-affinity, high dynamic range, genetically-encoded Ca²⁺ indicator, G-GECO1.2, to generate TPC1–G-GECO (TPC1–GG; Fig. 8A). The *tpcn1–GG* mRNA was injected into embryos at the one-cell stage, and primary cultures were then prepared at ∼48 hpf. Co-injection of *tpcn1–GG* mRNA with *mKate2–Lamp1* DNA allowed us to simultaneously assess late endosome and lysosome motility, morphology and interactions alongside Ca²⁺ signaling events in cultured SMCs (Fig. 8Ba). A time series of confocal images of a representative cultured SMC expressing TPC1–GG and mKate2–Lamp1 demonstrated LNP Ca²⁺ events associated with endolysosomal dynamics that occur during possible membrane contact events (Fig. 8Bb–Bg). To confirm the validity of our TPC1–GG reporter construct, SMCs were exposed to extracellular Ca²⁺ via treatment with ionomycin and CaCl₂ (black arrows in Fig. 8Ca, and Fig. 8Cb–Cd) such that the TPC1–GG sensor was saturated, as seen by the yellow color in Fig. 8Cd, and via the elevated relative G-GECO1.2 signal intensity (%G-GECO1.2$_{max}$) shown in the line graph (Fig. 8Ca). The number of detectable TPC1–GG-generated LNP Ca²⁺ fluorescence events was quantified at the cell ends as a percentage of the total number of TPC1–GG detected events recorded during the entire time-lapse series (i.e. both before and after the addition of ionomycin and CaCl₂; Fig. 8Da). The Ca²⁺-specificity of the TPC1–GG sensor was demonstrated by buffering Ca²⁺ levels in SMCs using cell-permeable BAPTA-AM or dimethyl-BAPTA-AM (DMB-AM), whereas the nicotinic acid adenine dinucleotide phosphate (NAADP)-specificity of the sensor was demonstrated via treatment with the NAADP antagonist, *trans*-Ned-19. Our data showed that pretreatment of cells with BAPTA-AM, DMB-AM or *trans*-Ned-19 significantly attenuated the number of TPC1–GG puncta at the cell ends when compared with the number of puncta in untreated cells (Fig. 8Da). However, significantly more puncta were observed following treatment with DMB-AM (K_d=0.44 μM) than with BAPTA-AM (K_d=0.70 μM; Pethig et al., 1989). Application of a mutated TPC1–GG (TPC1^{L264P}–GG) also significantly reduced the number of puncta recorded. Furthermore, the mKate2–Lamp1-labeled puncta were significantly larger following treatment with *trans*-Ned-19, BAPTA-AM or DMB-AM compared with those in untreated cells. However, in this case there was no significant difference when comparing the two Ca²⁺ buffers (Fig. 8Db). TPC1^{L264P}–GG also induced slight enlargement of these puncta, but the data were not significantly different from those obtained for the TPC1–GG control.

DISCUSSION

Endolysosomal Ca²⁺ channels

Considerable interest is building with regards to the intracellular signals generated by Ca²⁺ release from endolysosomes via the various Ca²⁺-release channels (including TPCs, MCOLN and P24X channels), that decorate their surface (Dong et al., 2010; Morgan and Galione, 2014; Huang et al., 2014; Marchant and Patel, 2015; Vassileva et al., 2020). This is in part due to the role these channels play in the regulation of endolysosomal trafficking and membrane contact events within cells, which in turn contributes to a plethora of cellular functions, including differentiation (Kelu et al., 2017), cell division (Horton et al., 2015) and membrane repair (Reddy et al., 2001). These Ca²⁺-release channels are distributed heterogeneously among different endolysosomes. They can also be activated by family-specific endogenous agonists, generate distinct Ca²⁺ signaling signatures, possess varying domains of cytoplasmic influence, and have either specific or general targets (Raffaello et al., 2016; Yang
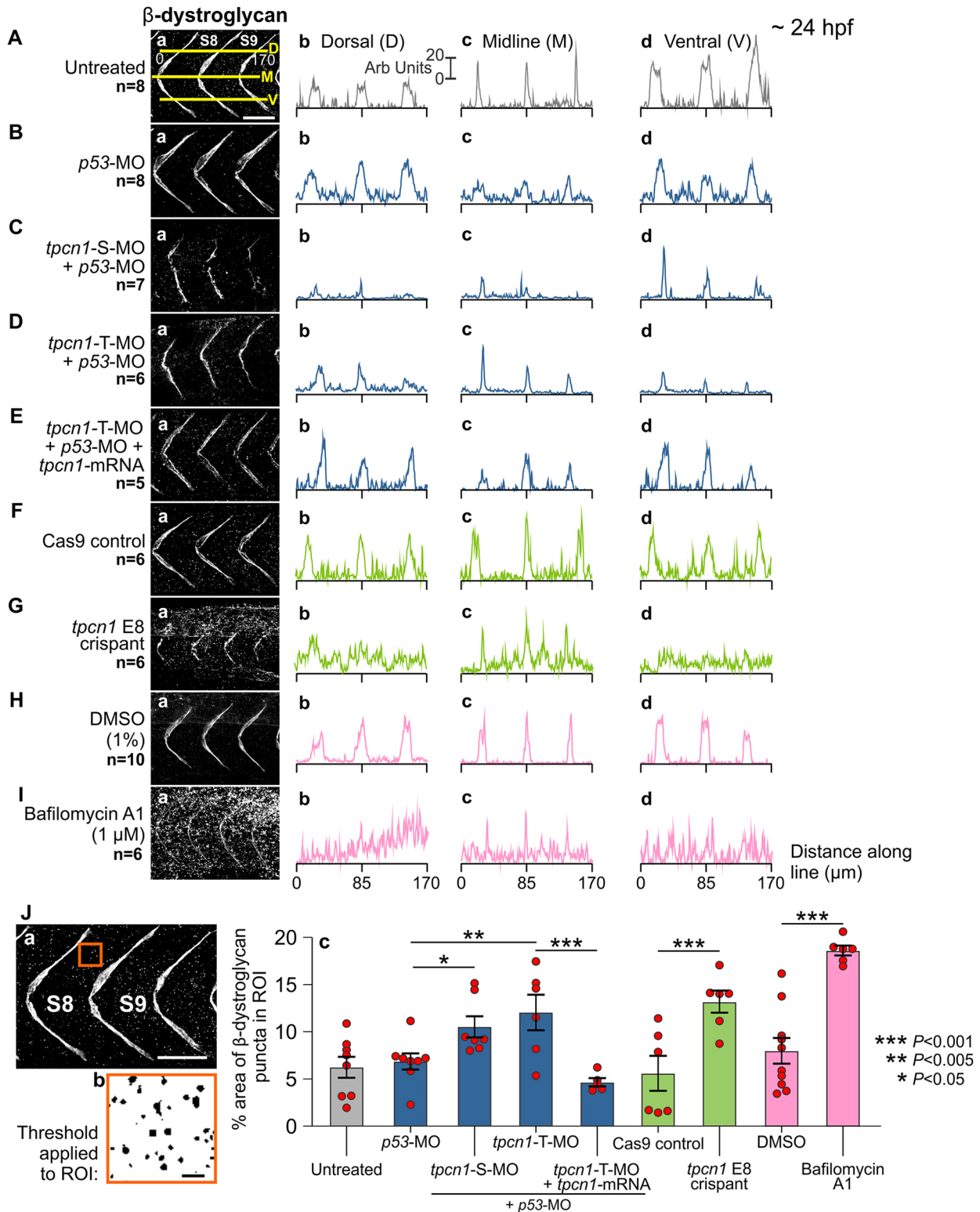
Fig. 6. Distribution of β-dystroglycan in *tpcn1* morphants, E8 crispants or following treatment of WT embryos with bafilomycin A1. (A–E) Embryos were (A) untreated; (B) injected with *p53*-MO alone; or injected with *p53*-MO and (C) *tpcn1*-S-MO, (D) *tpcn1*-T-MO or (E) *tpcn1*-T-MO plus *tpcn1* mRNA. (F,G) Representative (F) Cas9 control and (G) *tpcn1* E8 crispant. (H,I) Embryos were treated with (H) DMSO or (I) bafilomycin A1 at the indicated concentrations. Embryos in A–I were fixed at ~24 hpf, and β-dystroglycan was labeled. Images on the left are representative confocal *z*-stacks of lateral views showing somites (S) 8 and 9. In Aa, the yellow lines indicate the location of line scans conducted across the dorsal (D), midline (M) and ventral (V) regions of the trunk. Line-scan analysis graphs (panels b, c and d for D, M and V regions, respectively) show the relative fluorescence intensity of β-dystroglycan across the MJs shown in the confocal images (Arb units, arbitrary units). (Ja) Confocal image showing the region of interest (ROI, orange square) in the center of S8, and (Jb) an example of the ROI with a threshold applied to quantify the percentage area of β-dystroglycan-expressing puncta. (Jc) Bar graph showing mean±s.e.m. and individual data points of the percentage area of β-dystroglycan labeling for each treatment group in A–I. The data were compared using one-way ANOVA and Fisher's LSD test. Scale bars: 50 μm (Aa–Ja), 5 μm (Jb).
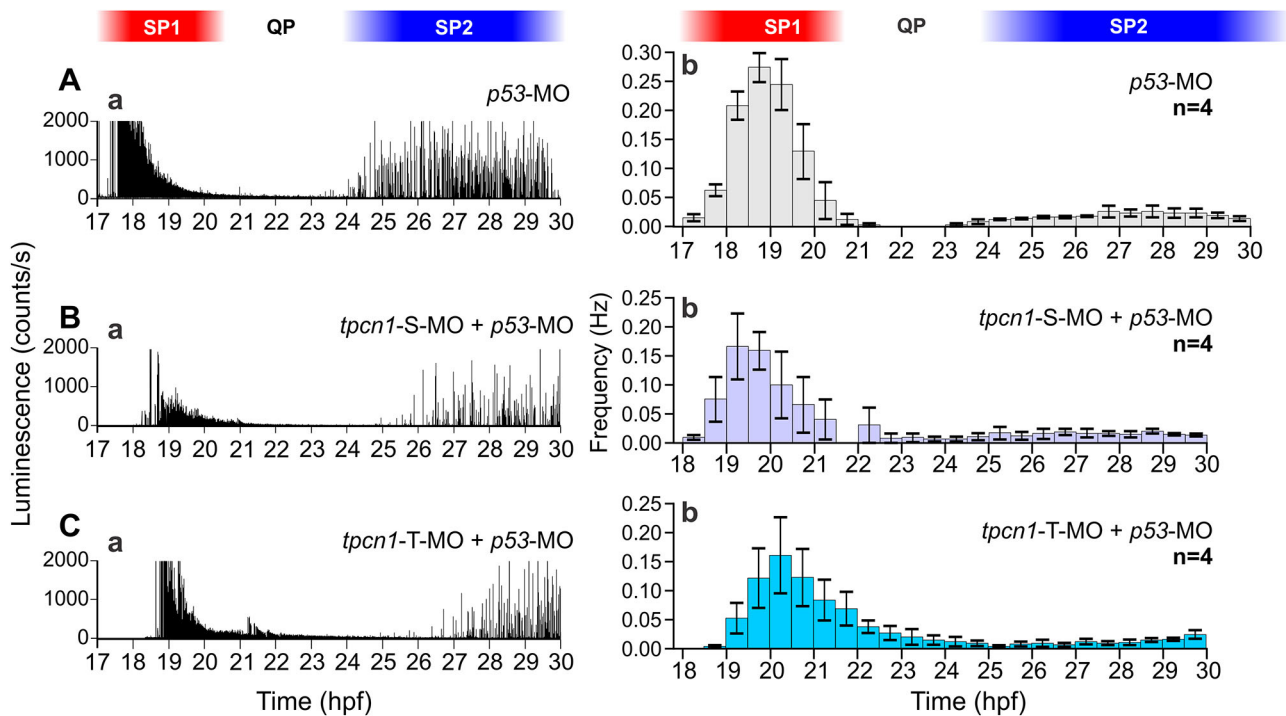
Fig. 7. Effect of MO-based knockdown of *tpcn1* on the Ca²⁺ transients generated in the trunk musculature detected via aequorin-based luminescence. (Aa,Ba,Ca) Representative temporal profiles of the luminescence generated by Tg(α-actin:aeq) embryos that were injected at the one- to four-cell stage with: (Aa) *p53*-MO alone, (Ba) *p53*-MO and *tpcn1*-*S*-MO, or (Ca) *p53*-MO and *tpcn1*-*T*-MO. (Ab,Bb,Cb) Histograms showing the mean±s.e.m. frequency of the Ca²⁺ transients generated every 30 min in the trunk musculature from ∼17–18.5 hpf to ∼30 hpf in embryos treated as described in Aa, Bb and Ca, respectively. Ca²⁺ signaling periods 1 and 2 (SP1 and SP2, respectively) and the Ca²⁺ signaling quiet period (QP) are shown.

et al., 2019). As such, they present a complex signaling interactome with multiple regulatory functions during development, physiology, homeostasis and disease (Zhu et al., 2010b; Marchant and Patel, 2015; Jin et al., 2020; Vassileva et al., 2020).

Attenuation of *tpcn1* results in abnormal SMC attachment phenotypes

Embryos with attenuated *tpcn1* expression appear to phenocopy reported zebrafish muscle disease models (Goody et al., 2017) with regards to (1) SMC detachment from the MJ (Fig. S1) and (2) SMC boundary crossing (Figs 1,2). In *tpcn1* morphants, these myoseptal and SMC abnormalities were most obvious at ∼48 hpf, suggesting that the integrity of the MJs might be progressively challenged during myotome development in these embryos. We propose that following the onset of more intense contractile activity during the hatching phase starting at ∼48 hpf (Saint-Amant and Drapeau, 1998), the forces generated might expose weaknesses in the SMC myoseptal attachments. This results in the abnormal SMC detachment phenotypes we observed in the morphants, mutants and E8 crispants. Our *tpcn1* morphant phenotypes resemble other zebrafish models following knockdown or knockout of cell–ECM adhesion components such as integrin α7 or dystroglycans (Gupta et al., 2011; Goody et al., 2012). Given that endolysosomal trafficking in ECM formation and remodeling is well documented (Moreno-Layseca et al., 2019), this suggests a possible role for TPC1-mediated Ca²⁺ release in regulating the trafficking of these essential ECM components to the forming MJ. This is followed by the maintenance of junction integrity and stability once trunk contractions begin.

The myotome boundary-crossing phenotype we and others have observed in zebrafish morphants and mutants, resembles that of

various related human myopathies (Henry et al., 2005; Goody et al., 2017). Some of these mutated genes express key components of the ECM and the DAPC that are essential for the formation of the MJ. We suggest, therefore, that Ca²⁺ released via TPC1 might be involved in regulating membrane contact events essential for trafficking and depositing required components to the MJ, and as a result contribute to the termination of SMC elongation, described as fiber 'capture' (Goody et al., 2017). We noted a paucity of abnormal phenotypes in the *tpcn1* mutants compared with the morphants. Similar discrepancies between other mutants and morphants have been reported before in zebrafish (Rossi et al., 2015). However, we demonstrated a closer reproducibility in the phenotypes of the *tpcn1* F₀ E8 crispants and morphants (Figs 1,2).

The vertical myosepta form from the early somite boundaries, which develop in the paraxial mesoderm during the segmentation stage (Kimmel et al., 1995; Henry et al., 2000). We found that these somite boundaries still developed in the *tpcn1* morphants (Fig. S6A). These observations are supported by a previous report showing that no regular Ca²⁺ transients are generated during the formation of the rostral–caudal somite boundary (Leung et al., 2009). Furthermore, local uncaging of a photolabile Ca²⁺ buffer (Diazo-2) in the paraxial mesoderm just prior to the onset of somite formation does not inhibit the formation of the rostral–caudal somite boundary, although the extension of the lateral somite boundary is abnormal compared with that of controls (Leung et al., 2009). These data suggest that rostral–caudal somite boundary formation does not require a Ca²⁺ transient generated by release via any Ca²⁺ channel (including TPC1). We suggest, therefore, that the myotome boundary-crossing phenotype we observed at 48 hpf when *tpcn1* expression was attenuated is not due to the absence of a rostral–caudal somite boundary. Rather, we propose that the lack of capture
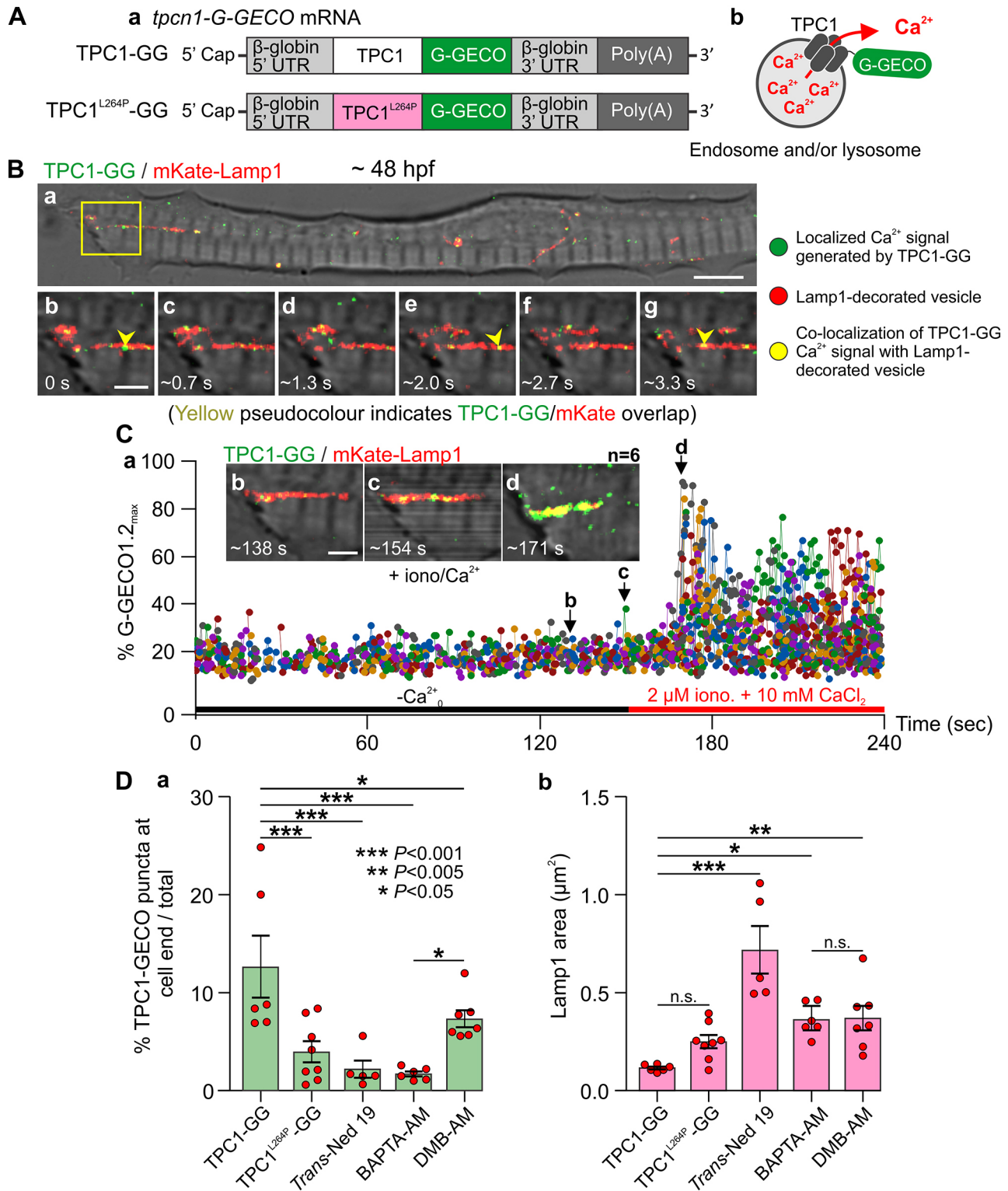
Fig. 8. See next page for legend.

of SMCs is due to the absence of an essential MJ component (or components) that are delivered to the forming MJ in a TPC1-dependent manner.

We have previously shown that in *tpcn2* morphants and mutants, despite the pan-cellular SP1 and SP2 Ca^{2+} transients being completely inhibited and the myofibrillar structure disrupted, SMCs remain attached to the MJ and no SMC myotome

boundary crossings are observed (Kelu et al., 2017). However, a somewhat opposite situation was observed in the *tpcn1* morphants, mutants and E8 crispants, where the most prominent abnormal features were the detachment of some SMCs at the MJ and myotome boundary crossover by others. Furthermore, myofibrillogenesis was also relatively normal (Fig. 1). A somewhat similar situation has been reported following complete inhibition of pan-cellular

Fig. 8. Visualization of highly localized TPC1–G-GECO-generated Ca^{2+} transients associated with Lamp1-labeled vesicles in cultured SMCs. (Aa) Design of *tpcn1–G-GECO* (control) and dominant-negative *L264P-tpcn1–G-GECO* constructs, which encode TPC1–G-GECO (TPC1-GG) and TPC1^{L264P}–G-GECO (TPC1^{L264P}-GG), respectively. (Ab) Schematic to show TPC1-GG in the endolysosome membrane and the flux of luminal Ca^{2+} through TPC1. (Ba–Bg) Confocal images of a representative SMC isolated from a ~48 hpf embryo that had been injected with mRNA encoding TPC1-GG (green) and DNA encoding mKate2-tagged Lamp1 (red). Regions of colocalization are yellow. The region bounded by the yellow rectangle in Ba is shown at higher magnification in Bb–Bg, which are individual frames captured from a confocal time series showing the punctate appearance of TPC1-GG fluorescence associated with Lamp1-positive organelles close to the end of the SMC (yellow arrowheads in Bb, Be and Bg). Images are representative of six cells over three experiments (each experiment consisting of >20 embryos). (Ca) Line graph showing tracked TPC1-GG puncta and their relative fluorescence intensity (expressed as a percentage of maximum intensity; distinct puncta are shown in different colors) in the time series shown in B, during which the cell was bathed in Ca^{2+}-free medium (–Ca$^{2+}_o$, indicating no Ca^{2+} on the outside) and then subsequently treated with 2 µM ionomycin and 10 mM CaCl$_2$ to saturate TPC1-GG. Arrows b, c and d indicate frames shown in panels Cb, Cc and Cd, respectively. (Cb–Cd) Individual frames from the same time series showing TPC1-GG and mKate2–Lamp1 fluorescence at the cell end (Cb) before, (Cc) during and (Cd) after the addition of ionomycin and CaCl$_2$. (D) Bar charts showing the mean±s.e.m. and individual data points of (Da) the quantification of TPC1-GG-detected Ca^{2+} signals and (Db) the area of Lamp1-labeled puncta at the ends of SMCs. Regarding the former, values were expressed as a percentage of the TPC1-GG puncta at the cell ends before all the available GG-sensors were saturated (i.e. before permeabilization with ionomycin and CaCl$_2$), out of the total number of TPC1-GG puncta in the cell after permeabilization. The embryos had been injected with plasmids encoding mKate2-tagged Lamp1 and either *tpcn1-GG* mRNA or *tpcn1^{L264P}-GG* mRNA. In some experiments the former were treated with 100 µM *trans*-Ned-19, 25 µM BAPTA-AM or 25 µM dimethyl-BAPTA-AM (DMB-AM). *n*=5–8. The data in D were compared using one-way ANOVA and Fisher's LSD test (n.s., not significant). Scale bars: 5 µm (Ba), 2 µm (Bb–Bg and Cb–Cd).

cytosolic Ca^{2+} signals in macrophages; localized TPC-dependent Ca^{2+} nanodomains are still generated and the cells are able to phagocytose IgG-coated fluorescent beads (Davis et al., 2020). This supports the suggestion that TPC-isoform-specific Ca^{2+} signals regulate distinct cellular activities.

In addition to TPCs, other Ca^{2+}-release channels, including MCOLN and P2X4 channels, are expressed in endolysosomes (Dong et al., 2010; Cheng et al., 2014; Huang et al., 2014; Li et al., 2017), and orthologs of these genes have been found in zebrafish (Diaz-Hernandez et al., 2002; Li et al., 2017). However, when two *mcoln1* genes were knocked out in zebrafish, although there was a progressive abnormal accumulation of autophagosomes in the skeletal muscle fibers, no effect was reported regarding sarcomeric assembly and myofibrillogenesis, or the localization of vinculin (a key cell–matrix adhesion protein) at the MJ (Li et al., 2017). Furthermore, no SMC detachment or myotome boundary crossing was reported from the *mcoln1* mutants. This is unlike our *tpcn1* morphants and mutants, where SMC detachments and boundary crossing were observed (Fig. 1). The findings reported by Li et al. (2017) indicate that in *mcoln1* mutants some aspects of endolysosomal trafficking and membrane contact activity are normal whereas others are not. These results suggest that the Ca^{2+}-signaling signature generated via MCOLN1 might be distinct and thus have different functions than Ca^{2+} released via TPC1 in SMCs.

Trafficking and localization of TPC1-decorated endolysosomes in SMC MJs

The localization of endolysosomes near the SMC MJs in intact zebrafish (Fig. 3A,B), resembles that reported in isolated rat myotubes (Kaisto et al., 1999). The range of velocities recorded for TPC1-labeled vesicles undergoing transport away from or towards the MJ (Fig. 3D) is within the range of velocities previously reported for dynein-mediated retrograde vesicle transport (Granger et al., 2014) and kinesin motor family-mediated anterograde vesicle transport (Arpağ et al., 2014), respectively.

Microtubules (in conjunction with plus-end- or minus-end-directed motors) are known to play a major role in endolysosomal trafficking (Granger et al., 2014). The visualization of microtubules in cultured SMCs and treatment with nocodazole showed that this is also the case with regards to TPC1-labeled vesicles (Fig. 4C). Our results indicate that at the ends of SMCs, TPC1-labeled vesicles move with variable velocity, but slow as they approach the MJ (Fig. 4D). In other systems it has been proposed that this might be due to elements of the cytoskeleton impeding the movement of trafficking vesicles, resulting in them slowing and/or pausing at microtubule intersections (Zajac et al., 2013; Verdeny-Vilanova et al., 2017). Furthermore, in the cortical region of cells, the anterograde microtubule-based transport system transfers trafficking vesicles to the actin cytoskeleton for final delivery to the plasma membrane (Granger et al., 2014). This same process then acts in reverse to pass endocytosed vesicles to the microtubule system for retrograde transport. In SMCs, elements of the cortical actin cytoskeleton are also responsible for attaching terminal sarcomeres (via dystrophin) to the DAPC and ultimately to laminins in the ECM (Ervasti and Campbell, 1993). This terminal actin structure can be clearly seen in Figs 1Baii and 3F. We suggest, therefore, that at the ends of the SMCs near the MJ, a combination of vesicle size, intersecting microtubules and the cortical actin cytoskeleton act together to reduce the velocity of vesicles in either direction.

The introduction of *tpcn1*-S-MO or *tpcn1*-T-MO had a significant deleterious effect on both the distribution (Fig. 5Haii and size (Fig. 5Hb) of endolysosomes. However, in the case of the *tpcn1*-T-MO, both aspects could be rescued via the introduction of a *tpcn1*-mRNA, indicating the specificity of the MO-based knockdown. Our observations regarding the distribution and size of endolysosomes are consistent with other reports where the expression of *tpcn1* was attenuated (Kilpatrick et al., 2017), and the morphology and localization of endolysosomes were disrupted (de Araujo et al., 2020). Thus, our new data in zebrafish support a previously proposed role for TPC1 in the normal functioning of the endolysosomal trafficking network (Vassileva et al., 2020).

We co-expressed zebrafish TPC1 with a variety of endolysosomal markers (Castonguay et al., 2017; Hall et al., 2020) and showed that at the end of SMCs near the MJ, TPC1 appeared to populate the membranes of early endosomes and of late endosomes and lysosomes (Fig. 4Ae). These findings support previous reports indicating the broad distribution of TPC1 in the endolysosomal system (Morgan and Galione, 2014). In addition, as reported from other cell types (Raiborg et al., 2015), TPC1-labeled endosomes were closely associated with the SR throughout SMCs. They were especially prevalent around the nucleus of primary cultured SMCs (Fig. 4Ba) but were also found at the ends of these cells, which would normally form the MJ *in vivo* (Fig. 4Bb). Such endolysosomal–ER and endolysosomal–SR contact sites are currently the subject of considerable interest with regards to the maturation of endolysosomes and intraorganellar signaling (Cremer et al., 2020; Huang et al., 2020). Furthermore, it has been suggested that localized TPC-mediated Ca^{2+} release might play a key role in regulating such membrane contact site activity (Kilpatrick et al., 2017; Vassileva et al., 2020).

Localization of β-dystroglycan at MJs

As attenuation of *tpcn1* expression resulted in SMC detachment from the vertical myosepta (Fig. 1), we hypothesized that vesicle cargoes transported by endolysosomes to the MJ might include key components of the DAPC and/or the ECM. We chose, therefore, to explore what the disruption of TPC1-mediated Ca^{2+} signaling activity might have on the distribution of β-dystroglycan, a key transmembrane component of the DAPC (Parsons et al., 2002). The mislocalization of β-dystroglycan following TPC1 attenuation in ∼24 hpf embryos (Fig. 6), is comparable to that observed in zebrafish models of dystroglycanopathies (Gupta et al., 2011). As the successful capture and attachment of SMCs at the MJ likely involves trafficking and localization of additional DAPC components, as well as other transmembrane linkage protein complexes and ECM constituents (Goody et al., 2012, 2017), further investigation is required to identify which of these might also be regulated by TPC1-generated LNP Ca^{2+} transients.

Comparing TPC1-mediated and TPC2-mediated Ca²⁺ release

We have previously published a series of papers showing that Ca^{2+} released via TPC2 acts to trigger a series of pan-cellular Ca^{2+} signals that are essential for specific myogenic events during the differentiation of SMCs in zebrafish embryos (Kelu et al., 2015, 2017, 2019). When the activity of TPC2 is attenuated in morphant or mutant embryos, or in wild-type embryos treated with *trans*-Ned-19 or bafilomycin A1, these pan-cellular signals are significantly inhibited and myofibrillar organization is extensively disrupted (Kelu et al., 2015, 2017). These observations suggest that following attenuation of TPC2 activity, there is no compensation by other Ca^{2+}-release channels resident in the endolysosomal or other organellar membranes (El-Brolosy and Stainier, 2017). The fact that the pan-cellular Ca^{2+} transients showed no significant attenuation following MO-mediated *tpcn1* knockdown (Fig. 7) supports the proposition that TPC isoforms have distinct signaling functions. Thus, although TPC2 generates pan-cellular propagating Ca^{2+} signals via a triggering process, TPC1-mediated Ca^{2+} release generates LNP Ca^{2+} transients similar to those described in other cell types (Ruas et al., 2010; Zhu et al., 2010a; Davis et al., 2020; Jin et al., 2020). Therefore, both TPCs can function within the endolysosomal system of the same SMC to regulate different myogenic processes that respond to distinct Ca^{2+} signaling signatures. Although attenuation of *tpcn1* expression had no significant effect on the SP1 and SP2 signaling signature once SP1 was initiated, there was a substantial delay of ∼1 h before the onset of SP1 in the morphants compared with the control embryos (Fig. 7). As both the *tpcn1*-T- and *tpcn1*-S-MO were injected into embryos at the one- to four-cell stage, the attenuation of *tpcn1* expression might have affected an earlier developmental event requiring TPC1-mediated signaling, resulting in the SP1 and SP2 delay observed. As the delay was not the focus of this paper, however, this suggestion remains essentially speculative and requires additional experimentation to resolve its cause.

Visualization and characterization of localized TPC1-generated Ca²⁺ transients

Given that the attenuation of *tpcn1* expression did not appear to affect the pan-cellular SMC Ca^{2+} signals (Fig. 7), we utilized TPC1–GG (Fig. 8; Zhao et al., 2011), which revealed that TPC1 generated LNP Ca^{2+} transients in SMCs. These findings were further confirmed via the use of TPC1^{L264P}–GG (to attenuate TPC1 activity) or via treatment of cultured SMCs with the NAADP antagonist *trans*-Ned-19, or with the Ca^{2+} buffers BAPTA-AM or

DMB-AM, all of which significantly reduced the number of GG-detected LNP Ca^{2+} events at the end of cultured SMCs (Fig. 8Da). The fact that treatment with *trans*-Ned-19 also resulted in a significant increase in the mean area of individual Lamp1-decorated vesicles (Fig. 8Db), supports our finding that following *tpcn1* knockdown there is an increase in the area (and altered morphology) of LysoTracker-stained puncta (Fig. 5Hb). Such a change in vesicle size indicates abnormal endolysosomal homeostasis (de Araujo et al., 2020). When comparing the effect of the same concentration of DMB-AM and BAPTA-AM, which have de-esterified dissociation constants (K_d) of 0.44 μM and 0.70 μM, respectively (at pH 7.0, 1 mM Mg^{2+} and 300 mM KCl; Pethig et al., 1989), the former had less of an effect on reducing the percentage of localized Ca^{2+} signaling events than the latter (Fig. 8Da). This suggests that the changes observed with BAPTA-AM were due to the faster buffering of the localized Ca^{2+} transients rather than a possible inhibitory side-effect of introducing the Ca^{2+} buffer. Similar results regarding the effectiveness of Ca^{2+} buffers with respect to their dissociation constants have been reported from several systems where a localized elevation of cytosolic Ca^{2+} has been found to be a required intracellular signal (Speksnijder et al., 1989; Davis et al., 2020; Guo et al., 2020). These findings suggest that LNP Ca^{2+} release by TPC1 might contribute to required endolysosomal dynamics and membrane contact events in the vicinity of the MJ in SMCs.

Previous reports provide clear evidence of a role for TPCs in endolysosomal trafficking (Marchant and Patel, 2015; Vassileva et al., 2020), and analysis of the TPC interactome has revealed an association between TPCs and Ca^{2+}-sensitive proteins including annexins, Rab proteins and SNARE proteins (Moccia et al., 2021). All of these are known mediators of membrane fusion, which regulates contact sites between endocytic vesicles and the ER (Eden et al., 2016). Several other studies have used BAPTA to show that localized TPC-evoked Ca^{2+} signals are likely mediators of endolysosomal trafficking events (Lin-Moshier et al., 2014; Grimm et al., 2017), and it has been proposed that Ca^{2+} release via TPCs provides a localized Ca^{2+} signal that regulates the fusion of closely apposed endolysosomal structures (Marchant and Patel, 2015).

Summary

We suggest that LNP TPC1-generated Ca^{2+} release helps regulate (with higher fidelity than pan-cellular TPC2-mediated Ca^{2+} release) key localized aspects of endolysosomal trafficking and membrane contact activity, which plays a critical role in SMC capture and attachment at the MJ. The generation of similar LNP Ca^{2+} events by TPCs has recently been reported to contribute to phagocytosis in macrophages (Davis et al., 2020). This suggests that LNP TPC-generated Ca^{2+} signals at membrane contact sites might be a common feature among different cell types and in different species. It has been proposed that endolysosomes constitute an active signaling interactome required to regulate intracellular trafficking (Marchant and Patel, 2015). We suggest that by expressing a diverse population of Ca^{2+}-release channels – each with their own family-specific endogenous agonists, Ca^{2+} signaling signatures and Ca^{2+}-sensitive targets – endolysosomes provide an additional level of regulatory complexity with regards to intracellular Ca^{2+} signaling. Thus, extending the elegant 'cellular Ca^{2+} signaling toolkit' proposition (Berridge et al., 2003), we suggest that endolysosomes possess their own 'organellar Ca^{2+} signaling toolkit', which interacts discerningly with other signaling elements to regulate a variety of cellular processes required for the development, maintenance and function of SMCs.

MATERIALS AND METHODS

Zebrafish husbandry

The AB and ABTU wild-type zebrafish strains were obtained from the Zebrafish International Resource Center (University of Oregon, Eugene, OR, USA) and Prof. Han Wang (Soochow University, Suzhou, China), respectively, whereas the α-actin-apoeaquorin-IRES-EGFP [*Tg(α-actin: aeq)*] line was previously developed in the Miller laboratory (Cheung et al., 2011). The fish were kept in AHAB systems (Pentair Aquatic Eco-Systems, Apopka, FL, USA) and their fertilized eggs were obtained and maintained at ~28°C using well-established protocols (Westerfield, 2000). All the procedures used in this study were conducted in accordance with the guidelines and regulations outlined by the Animal Ethics Committee of HKUST, and the Department of Health, Hong Kong.

In vivo reconstitution of aequorin and bioluminescence detection

To detect endogenous Ca^{2+} signals generated during embryogenesis, *Tg(α-actin:aeq)* embryos were incubated with *f*-coelenterazine (NanoLight® Technologies, Pinetop, AZ, USA) to reconstitute active aequorin (Shimomura, 1997). Coelenterazine was prepared and incubated with the embryos as described previously (Kelu et al., 2015). The embryos were placed in grooves made in 1% agarose within individual custom-built imaging chambers and then transferred to a Photon Multiplier Tube (PMT)-based system (Science Wares, Inc., MA, USA) for luminescence detection, as described previously (Cheung et al., 2011; Kelu et al., 2015).

Design and injection of MOs

All the MOs (Gene Tools LLC, Philomath, OS, USA) were prepared at a stock concentration of 1 mM in Milli-Q water and stored at room temperature. The expression of TPC1 was attenuated using splice (S)- or translation (T)-blocking *tpcn1* MOs. The *tpcn1*-S-MO was designed by us (with advice from Gene Tools), whereas the *tpcn1*-T-MO was designed by Dr. John Parrington (University of Oxford, UK). To evaluate the specificity of the *tpcn1*-T-MO by visualization of TPC1–EGFP fluorescence, embryos were co-injected with 2 ng *tpcn1*-T-MO plus 2 ng *p53*-MO into the yolk and ~150 pg of *tpcn1–EGFP* mRNA into the blastodisc. The design and synthesis of this fluorescently tagged TPC1 construct is described in the section below titled 'Design, cloning and injection of fluorescently tagged TPC1 constructs'.

Information about the protocols used to assess the knockdown efficiency of the *tpcn1*-S-MO is provided in the following sections (see 'Total RNA isolation and cDNA synthesis' and 'Total RNA isolation and RT-PCR to assess the knockdown efficiency of the *tpcn1*-S-MO').

To avoid possible off-target effects of the *tpcn1* MOs on p53 activity, each was co-injected with a *p53*-MO (Robu et al., 2007). The *p53*-MO (injected alone) and a standard control MO were also used as specificity controls (Kelu et al., 2015). The MOs were prepared and injected into AB wild-type embryos using methods described previously (Webb and Miller, 2013; Kelu et al., 2015). The sequences of the standard control MO and *p53*-MO are as described previously (Kelu et al., 2017), whereas those for the *tpcn1* MOs were as follows: *tpcn1*-S-MO: 5′-GTAGCGGATCAGATAATGACCTGCA-3′ and *tpcn1*-T-MO: 5′-TCCGCCATCCCGCAGAACCAAGACT-3′. The optimal injection dose of each MO was selected by evaluating the phenotypic dose response. Therefore, ~1 nl of the standard control MO (~5 ng), *p53*-MO (~5 ng), *tpcn1*-S-MO plus *p53*-MO (at a 1:1 ratio of each of ~2.5 ng, ~5 ng or ~8 ng), or *tpcn1*-T-MO plus *p53*-MO (at a 1:1 ratio of each of ~1 ng, ~2 ng or ~5 ng) was injected into the yolk of embryos at the one- to four-cell stage. In some experiments, embryos were co-injected with 2 ng *tpcn1*-T-MO plus 2 ng *p53*-MO and 50 ng or 100 pg *tpcn1*-mRNA.

Total RNA isolation and cDNA synthesis

Embryos were dechorionated manually at ~24 hpf or ~48 hpf using a pair of watchmaker's forceps (No. 5; Regine Switzerland SA, Morbio Inferiore, Switzerland). To prepare cDNA, total RNA was extracted by homogenizing 40 embryos in TRIzol reagent (Ambion, Invitrogen Corp., CA, USA) by trituration through a P200 pipette tip. Samples were kept at −80°C until

RNA isolation using the protocol provided with the TRIzol reagent. In brief, RNA was extracted with chloroform and precipitated using isopropanol. To isolate RNA, samples were centrifuged (at 12,000 *g* for 10 min at 4°C), and the resulting pellets were washed with 75% ethanol, after which they were centrifuged again (at 7500 *g* for 5 min at 4°C) and then resuspended in nuclease-free water. Subsequently, RNA was subjected to RT-PCR using random primers and the High-capacity cDNA Reverse Transcription kit (Applied Biosystems, Waltham, MA, USA) to synthesize cDNA.

Total RNA isolation and RT-PCR to assess the knockdown efficiency of the *tpcn1*-S-MO

RNA was isolated from 40 whole AB wild-type embryos at ~24 hpf that were either untreated or injected with the standard control MO, *p53*-MO, or *tpcn1*-S-MO plus p53-MO, and cDNA was synthesized as described above. PCR was performed on cDNA using the following primer pairs to assess the outcome of steric inhibition of the *tpcn1*-S-MO on the pre-mRNA transcript of *tpcn1*:

(1) A forward (splice-F) and reverse (splice-RI) primer pair was designed to amplify a 319 bp amplicon from wild-type *tpcn1*-mRNA. If the *tpcn1*-S-MO led to exon 2 being skipped (which we considered to be the most likely outcome produced by splice-blocking MOs), then the size of this amplicon was expected to be reduced to 123 bp. Splice-F, 5′-CTTATCCTGACCTGGGACGATG-3′ (targeting a region on exon 1); splice-RI, 5′-AGAGGGACAGGAGCATGAGTAAC-3′ (targeting a region on exon 3).

(2) Another reverse primer, targeting a region on exon 2 (splice-RII), was designed to verify the splice-F+splice-RI outcome. If exon 2 was skipped in the aberrantly spliced *tpcn1* mRNA, then a reduction in the level of the amplicon (178 bp) produced by the splice-F+splice-RII primer pair would be the expected result. Splice-RII, 5′-GGTATATTGCTGCTTCTTGGAAGTT-3′.

(3) Given that the splice-F+splice-RI primer pair produced a band of greater size by agarose gel electrophoresis, and because the splice-F+splice-RII primer pair generated equivalently strong bands in all the samples, it was deduced that exon skipping did not occur upon injection of the *tpcn1*-S-MO. For this reason, another reverse primer was designed to detect intron inclusion: splice-RIII, 5′-CCTGAACTGAGTGTGTGTTGG-3′. Splice-RIII targeted a region on intron 2, and the amplicon produced by splice-F+splice-RIII was expected to be 255 bp.

β-actin primers were used as an internal control in these experiments. The PCR cycling parameters comprised 30 s denaturation at 95°C, 30 s annealing at 58°C and 30 s elongation at 72°C. All the amplicons were analyzed using 1% agarose gel electrophoresis.

Design, cloning and injection of the mRNA rescue construct

To validate the effects of the *tpcn1*-T-MO, embryos were injected with a rescue construct comprising a *tpcn1-202* mRNA that lacked the MO recognition site (Eisen and Smith, 2008). To prepare the rescue mRNA, *tpcn1-202* was cloned from cDNA using custom primers designed to incorporate silent mutations to avoid MO recognition at the start codon. The primer sequences used for PCR amplification were as follows: rescue-F, 5′-<u>AATT</u>**GGTACC**CATGGC*A*GA*T*GGGGACGACGAC-3′; rescue-R, 5′-GGCC**CTCGAG**TTAGTTAATGCTGTTTGTGGCACC-3′. The leader sequences (to optimize restriction enzyme digestion) are underlined; restriction enzyme sites for KpnI and XhoI (New England Biolabs Inc., MA, USA) are shown in bold, and silent mutations are shown in italics. PCR was performed using the Phusion® High-Fidelity DNA Polymerase (New England Biolabs Inc.) with an initial 30 s denaturing step at 98°C, followed by 35 cycles of a 5 s denaturation step at 98°C and a 75 s annealing and extension step at 72°C. This was followed by a final elongation step at 72°C for 5 min. The amplicons were analyzed via 1% agarose gel electrophoresis. They were then purified using a PCR-M Clean Up System (Viogene BioTek Corp., Taipei, Taiwan) and cloned into the pSP64TNE expression vector (Addgene, MA, USA) using a T4 DNA ligase (Thermo Fisher Scientific, Inc., CA, USA). The results were confirmed by Sanger Sequencing (BGI, Shenzhen, China).

To prepare mRNA, the pSP64TNE-*tpcn1-202* plasmid was linearized with SmaI (New England Biolabs Inc.), and *in vitro* transcription was

performed with a mMESSAGE mMACHINE SP6 transcription kit (Ambion). The mRNA was then purified using phenol-chloroform extraction (Sambrook and Russell, 2006) and diluted to ∼200 ng/µl in RNase-free water for storage at −80°C. During rescue experiments, embryos at the one-cell stage were injected in the yolk with ∼2 ng tpcn1-T-MO+∼2 ng p53-MO, after which they were injected in the blastodisc with ∼50 ng or ∼100 pg tpcn1-mRNA.

Generation of *tpcn1* mutants and E8 crispants: design, synthesis and injection of gRNA and *Cas9* mRNA

To generate a *tpcn1* knockout zebrafish line and *tpcn1* E8 crispants, CRISPR/Cas9-mediated targeted mutagenesis was performed by injection of *Cas9* mRNA and sgRNAs against the *tpcn1* sequence following established protocols (Varshney et al., 2016). Two sgRNA sequences, targeting regions in exon 5 and exon 8, were chosen using the ZebrafishGenomics UCSC Genome Browser track (http://genome.ucsc.edu/cgi-bin/hgHubConnect) developed previously (Varshney et al., 2015). These targets are known to be common to all three of the known *tpcn1* splice variants and are predicted to have as few off-targets as possible. These exons lie within the first of two homologous six-transmembrane subunits (IS1–IS6 and IIS1–IIS6) that comprise the TPC dimer. Specifically, they encode the third transmembrane helices (IS3) within the voltage-sensing domain and a pore domain (IP), respectively.

To synthesize sgRNAs, an oligo-based method was used such that the target-specific oligos and an 80 nucleotide (nt) 'generic' DNA oligo were annealed and extended to create a template for *in vitro* transcription (Varshney et al., 2015). The 'generic' DNA oligo encodes the chimeric guide RNA (crRNA:tracrRNA) needed to generate the 'stem-loop' structure that is bound by the Cas9 nuclease (Cong et al., 2013).

The sequences of the target-specific oligos are as follows: sgRNA-E5, 5′-*GATCAC***TAATACGACTCACTATAgg**CTCTTGTGACGCGCAGGT*G-TTTTAGAGCTAGAAATAGC*-3′; sgRNA-E8, 5′-*GATCAC***TAATA-CGACTCACTATAgg**CGTATTCGAAGAATCGT*GTTTTAGAGCTAG-AAATAGC*-3′.

An sgRNA targeting the tyrosinase (*tyr*) gene was used as a positive control to assess the sgRNA design and the quality of the *Cas9* mRNA (Varshney et al., 2016); its sequence is as follows: sgRNA-*tyr*-ctrl, 5′-*GATCAC***TAATACGACTCACTATAgg**ACTGGAGGACTTCTG*G-TTTTAGAGCTAGAAATAGC*-3′.

For these three sequences, protective bases are shown in non-bold italics; the T7 promoter (17 nt) and minimal sequence, 'gg', for initiation are in bold; the target sites that precede an NGG protospacer adjacent motif (PAM; 15–18 nt) sequence are underlined (NGG not included in the actual sequence); and a 20-nt sequence complementary to the 'generic' guide RNA is in bold italic font. The sequence of the 'generic' DNA oligo/universal bottom-strand ultramer (Integrated DNA Technologies, IA, USA) is as follows, with the sequence complementary to the target-specific oligos shown in italics: 5′-AAAAGCACCGACTCGGTGCCACTTTTTCA-AGTTGATAACGGACTAGCCTTATTTTAACTT*GCTATTTCTAGCTCT-AAAAC*-3′.

To synthesize the sgRNAs, an oligo assembly reaction that contained 10 µM of either of the target-specific oligos and the 'generic' DNA oligo was annealed and extended using the Phusion® High-Fidelity DNA polymerase (New England Biolabs Inc.). The cycling conditions were 2 min denaturation at 98°C, followed by a 10 min annealing step at 50°C and a 10 min extension step at 72°C. The annealed oligos were then used as templates for *in vitro* transcription using the mMESSAGE mMACHINE™ T7 Transcription kit (Ambion), and RNA was purified using phenol-chloroform (as described above). The sgRNAs were run on a 2.5% agarose gel to verify successful RNA synthesis, and then diluted to ∼200 ng/µl in RNase-free water for storage at −80°C.

To synthesize *Cas9* mRNA, the pT3TS-nls-zCas9-nls plasmid (Jao et al., 2013) was first linearized using the XbaI restriction enzyme (New England Biolabs Inc.). Digestion was then verified by gel electrophoresis with a 1% agarose gel and purified using the Monarch® PCR & DNA Cleanup kit. An *in vitro* transcription reaction was then carried out using the mMessage mMachine T3 Transcription kit (Ambion), and the *Cas9* mRNA was purified using phenol-chloroform (as described above). Purified RNA was

run on a 1% agarose gel, which produced a band at ∼1.6 kb, indicative of successful *Cas9* mRNA synthesis. The RNA was diluted to ∼500 ng/µl in RNase-free water and divided into aliquots for storage at −80°C. Then, ∼100 pg sgRNA per target and 300 pg *Cas9* mRNA were injected into the blastodisc of ABTU wild-type embryos at the one-cell stage. Following injection with the *tyr* sgRNA, the reduced pigmentation in embryos at ∼48 hpf was indicative of successful mutagenesis.

Generation of *tpcn1* mutants: genotyping by HRMA

A combination of HotSHOT raw genomic extraction (Meeker et al., 2007) and HRMA (Samarut et al., 2016) was used at several stages in the workflow to establish the *tpcn1* mutant line (called *tpcn1^dhkz101^* in accordance with the ZFIN zebrafish nomenclature guideline; http://zfin.org). These are described as 'stages 1 to 4' in the following text. By modifying the source of genomic DNA, HRMA was used to rapidly assess mutagenic activity of the *Cas9* mRNA and the *tpcn1* sgRNAs in F_0 embryos (stage 1), as well as to identify CRISPR-induced indels in the F_1 adults (stage 2) and to perform genotyping in the F_2 embryos (stage 3) and adults (stage 4).

Genomic DNA was extracted from *tpcn1* mutant intact embryos and the caudal fin of adults. For the former, embryos were randomly selected and euthanized at ∼24 hpf, whereas for the latter a small region of the caudal fin (hereafter called a fin clip) was excised from adult fish after anesthetization in Danieau's solution (17.4 mM NaCl, 0.21 mM KCl, 0.12 mM $MgSO_4 \cdot 7H_2O$, 0.18 mM $Ca(NO_3)_2 \cdot 4H_2O$ and 1.5 mM HEPES; pH 7.2) containing ∼0.02% ethyl 3-aminobenzoate methanesulfonate (MS-222) (Westerfield, 2000). The embryos and fin clips were incubated in 50 mM NaOH for 20 min at 95°C, vortexed briefly and cooled to 4°C before the addition of 1/10 volume 1 M Tris-HCl (pH 8.0). To extract genomic DNA from the embryos (at stages 1 and 3), each embryo was placed in the well of a 384-well plate (LightCycler 480 Multiwell Plate 384, white; Roche Molecular Systems, Inc., CA, USA) containing 20 µl NaOH and 2.5 µl Tris-HCl, and then heated to 95°C in a Heratherm™ oven (Thermo Fisher Scientific Inc.). To extract genomic DNA from the fin clips (at stages 2 and 4), these were transferred to 1.5 ml microcentrifuge tubes (Axygen, Corning Inc., NY, USA) and heated to 95°C in a Thermolyne dry bath (Thomas Scientific, NJ, USA). The extracted DNA was either used immediately for HRMA or stored at 4°C. To perform HRMA, the genomic DNA of the sgRNA-injected embryos or adults was used as a template for an EvaGreen-based PCR reaction using the Precision Melt Supermix (Bio-Rad) and a LightCycler 480 instrument (Roche, Basel, Switzerland). Primers to amplify a ∼150–200 bp region surrounding the sgRNA target site of exon 5 or exon 8 were designed using the qPCR settings of Primer3 (http://www.bioinformatics.nl/cgi-bin/primer3plus/primer3plus.cgi). The primer sequences are as follows: HRMA-E5-F, 5′-TTGT-GTTTGGATTTGGTGCAC-3′; HRMA-E5-R, 5′-CTCCACAGTAACGG-CAGTCC-3′; HRMA-E5-F and HRMA-E5-R were expected to produce an amplicon of 192 bp. HRMA-E8-F, 5′-TATCAGCATGCCCCTGTTTG-3′; HRMA-E8-R, 5′-AGCTCGATGGACAGATACACG-3′; HRMA-E8-F and HRMA-E8-R were expected to produce an amplicon of 169 bp. To amplify these loci for HRMA at various steps in the generation of the stable *tpcn1* mutant line or *tpcn1* E8 crispants, a 10 µl reaction mixture was prepared for each sample, which consisted of 5 µl Precision Melt Supermix, 0.5 µl of each primer (10 µM), 2 µl genomic DNA and 2 µl MilliQ water. The reaction protocol for both PCR and HRMA on the LightCycler 480 instrument was as follows: initial denaturation for 2 min at 95°C, and then 45 cycles comprising a 10 s denaturation step at 95°C, a 30 s annealing step at 60°C, and a 20 s extension step. At the end of these 45 amplification cycles, there was a plate-read step at 72°C. Heteroduplex formation was performed with a 30 s denaturation step at 95°C and a 1 min annealing step at 60°C. Finally, melting and plate-read steps (20 readings/°C) were performed using a temperature ramp from 70°C to 95°C at 0.025°C/s, before finishing with a cooling step to 40°C for 30 s. Melt curve data of all the samples (including ABTU wild-type controls) were exported from the 'Melt Curve Genotyping' mode of the LightCycler® 480 SW 1.5.1 software (Roche, Basel, Switzerland), and uploaded to uAnalyze v2.1 (https://dna-utah.org/ua/uanalyze.html; Dwight et al., 2012). This software was used to normalize the data and plot difference curves for genotyping. Fish with CRISPR-induced indels in exon 5 were identified by analyzing shifts in their

melting curves from the wild-type samples. The genotyping results were confirmed by Sanger sequencing the F₁ progeny. To prepare samples for sequencing, PCR was performed on genomic DNA using the Rapid Taq Master Mix (Vazyme, Nanjing, China) and the following primers: HRMA-E5-F, 5′-TTGTGTTTGGATTTGGTGCAC-3′; HRMA-E5-genotyping-R, 5′-TGTTACCAACATCCGGTGAA-3′. These primers were used to amplify a 431 bp region surrounding the sgRNA target site of exon 5. PCR was performed with an initial 3 min denaturing step at 95°C, followed by 35 cycles comprising a 15 s denaturation step at 95°C, a 15 s annealing step at 51°C and a 10 s extension step at 72°C. These cycles were followed by a final elongation step at 72°C for 5 min. The amplicons were analyzed via 1% agarose gel electrophoresis. They were then purified using a Monarch® PCR and DNA Cleanup kit (New England Biolabs Inc.) and sequenced using the forward primer (HRMA-E5-F).

To identify indels from the sequencing data, the known genomic sequences of the wild-type samples and the potential mutants (containing double peaks in the chromatogram) were analyzed using Poly Peak Parser (http://yosttools.genetics.utah.edu/PolyPeakParser/; Hill et al., 2014). The selected *tpcn1* line containing a frameshift mutation (+16 bp) in exon 5 was then bred to generate a homozygous population.

To generate F₀ *tpcn1* E8 crispants, ~100 pg E8 sgRNA and ~300 pg *Cas9* mRNA were injected into ABTU embryos at the one-cell stage. At ~24 hpf and ~48 hpf, the E8 crispants were fixed, immunolabeled and imaged for phenotypic analysis. Subsequently, genomic DNA was extracted from individual embryos at ~48 hpf and HRMA was conducted to identify the presence of indels at the *tpcn1* locus. The cycling conditions used for HRMA and the subsequent analysis of melt curves were performed as described above.

Generation of *tpcn1* mutants: two-step RT-PCR
RNA was isolated from ABTU wild-type embryos as well as from *tpcn1* heterozygous and homozygous embryos at ~48 hpf. Experiments were conducted in triplicate, using 40 randomly selected embryos from one clutch for each. The extracted RNA was treated with TURBO DNase (Invitrogen) for 20 min at 37°C, and then ~1000 ng was reverse transcribed to produce cDNA, as described above. This was used as a template for amplification by PCR with the Rapid Taq Master Mix (Vazyme). The primers used are as follows: *tpcn1*-RTPCR-F, 5′-CGCAGAAACTTGAGGCAGATA-3′; *tpcn1*-RTPCR-R, 5′-CGTGTATCTGTCCATCGAGCT-3′. The amplicons were then separated by gel electrophoresis using 2% agarose gels.

Generation of *tpcn1* mutants: two-step qRT-PCR
RNA was extracted and treated with TURBO DNase, and then cDNA was synthesized, as described above. qRT-PCR was performed using the iTaq Universal SYBR Green Supermix (Bio-rad Laboratories, Inc., CA, USA) according to the manufacturer's instructions with three biological replicates and three technical replicates using 384-well plates. Two primers against *tpcn1* were designed, one targeting the exon 2–exon 3 junction, and the other spanning exons 22 and 23. Gene expression was analyzed using the $\Delta\Delta$Ct method (Livak and Schmittgen, 2001), and the relative level of *tpcn1* expression was compared to four reference genes: *actb2* (Tang et al., 2007), *mob4*, *lsm12b* (Hu et al., 2016) and *elfa* (also known as *eef1a1l2*; McCurley and Callard, 2008). The qRT-PCR primers used are as follows: *tpcn1*-qRTPCR-E2&3-F, 5′-GGAGGGAGAGAATAACGACAAG-3′; *tpcn1*-qRTPCR-E3-R, 5′-CAGAAGCTCCACCACATAGAA-3′; *tpcn1*-qRTPCR-E22-F, 5′-ACTGGAGCCGCCTTTATTT-3′; *tpcn1*-qRTPCR-E23-R, 5′-CTCTGTTCTTCCGGCTGTAAT-3′; *actb2*-F, 5′-CGAGCT-GTCTTCCCATCCA-3′; *actb2*-R, 5′-TCACCAACGTAGCTGTCTTT-CTG-3′; *mob4*-F, 5′-CACCCGTTTCGTGATGAAGTAC-3′; *mob4*-R, 5′-CAGCTCAGGCATCGCTTTC-3′; *lsm12b*-F, 5′-GTTGTCCCAAGCC-TATGCAATC-3′; *lsm12b*-R, 5′-TGATGTTCTTCTCCTGCCATTTAC-3′; *elfa*-F, 5′-CTTCTCAGGCTGACTGTGC-3′; *elfa*-R, 5′-CCGCTAG-CATTACCCTCC-3′.

Design, cloning and injection of fluorescently tagged TPC1 constructs
Fluorescently tagged TPC1 constructs were generated following existing protocols (Brailoiu et al., 2009; Castonguay et al., 2017), in which TPC1 was tagged at the C terminus with either an enhanced green fluorescent protein (EGFP) or tdTomato to avoid interfering with NAADP-sensitive motifs at the N terminus (Churamani et al., 2013). To generate these constructs, the full length *tpcn1* coding sequence was amplified from the pSP64TNE-*tpcn1-202* plasmid using a primer pair that omitted the stop codon and included a short linker. The resulting amplicon was cloned in-frame into the pSP64TNE-*EGFP* or pSP64TNE-*tdTomato* plasmids (Cheung et al., 2006) at the KpnI and AgeI site. The primer sequences used are as follows: forward primer *tpcn1*-fullcds-F, 5′-<u>TAAGCA</u>**GGTACC**AGACTATCCGTGTCCCCCAA-3′; reverse primer *tpcn1*-w/oSC-R, 5′-<u>TGCTAT</u>**ACCGGT**cc*GCCTCCGGA*GTTAATGCT-GTTTGTGGC-3′. The leader sequences are underlined; restriction sites for KpnI and AgeI (New England Biolabs Inc.) are in bold; and (in the reverse primer alone) the two additional bases included to ensure in-frame fusion are in lower case. When these two bases are combined with the bases shown in italics (i.e. cc*GCCTCCGGA*), they encode a short linker between TPC1 and the downstream fluorophore. mRNA encoding TPC1–EGFP or TPC1–tdTomato was synthesized as described above, and ~150 pg of this mRNA was injected into AB wild-type embryos at the one-cell stage.

Design, cloning and injection of GECO-tagged TPC1 constructs
To monitor highly localized endolysosomal-generated cytoplasmic Ca²⁺ domains, a low-affinity, high dynamic range genetically encoded Ca²⁺ indicator (G-GECO1.2, K_d 1.2 μM; Zhao et al., 2011) was tethered to the C terminus of TPC1. The CMV-GEM-GECO1.2 plasmid containing the G-GECO1.2 coding sequence, was obtained from Addgene (plasmid #32446). The coding sequence was fused in-frame behind previously generated pSP64TNE expression vectors containing wild-type *tpcn1* using Gibson assembly. A dominant-negative 'pore-dead' zebrafish TPC1 construct was also designed to reproduce the pore-dead TPC1 mutant generated by Brailoiu et al. (2009), which contains the L273P mutation in human TPC1. The protein sequences of human and zebrafish TPC1 were aligned using the constraint-based alignment tool (COBALT; Papadopoulos and Agarwala, 2007) and it was deduced that Leu264 in the zebrafish TPC1 protein sequence is the equivalent of Leu273 in the human sequence. Thus, a construct in which Leu264 of zebrafish TPC1 was substituted for proline was generated using mutagenic and outer primers. The mutagenic primer sequences are as follows:

tpcn1-L264P-F, 5′-ATTGTGAGT*CCT*TTCGTCCTC-3′; *tpcn1*-L264P-R, 5′-GAGGACGAA*AGG*ACTCACAAT-3′. The codon that substitutes leucine for proline is shown in italics.

The outer primer sequences (TPC1-fullcds-F and TPC1-w/oSC-R) are as described above. These primers were used to generate fragments with overlapping ends to be cloned into the pSP64TNE expression vector to create the pSP64TNE-*L264P-tpcn1* plasmid. Subsequently, the following primers were designed to amplify the G-GECO1.2 coding region from the CMV-GEM-GECO1.2 plasmid with overhangs for homology-based annealing: forward primer GECO-F, 5′-*CTCCGGAGGCGG*ACC-GGTCGCCACCatggtcgactcatcacgt-3′; reverse primer GECO-R, 5′-GGTAACCAGATCCGAATTCTttacttcgctgtcatcatttgtac-3′. Sequences that are complementary to the G-GECO1.2 coding sequence are in lowercase; those that overlap with the linearized pSP64TNE-*tpcn1* vectors are in uppercase, and the short linker sequence between TPC1 and G-GECO1.2 (in the forward primer) is shown in italics. PCR was performed using the Phusion® High-Fidelity DNA polymerase (New England Biolabs Inc.) with an initial 30 s denaturing step at 98°C, followed by 35 cycles of a 5 s denaturation step at 98°C, a 20 s annealing step at 61°C and a 20 s extension step at 72°C. This was followed by a final elongation step at 72°C for 8 min. The amplicons were analyzed by 1% agarose gel electrophoresis. They were then purified using a Monarch® DNA gel extraction kit (New England Biolabs Inc.). Fragments containing *tpcn1* or mutagenic *tpcn1* were amplified from the pSP64TNE-*tpcn1* or pSP64TNE-*L264P-tpcn1* plasmid using the following primers to create overlapping ends with the G-GECO1.2 fragment: forward primer SP6-F: 5′-AGAATTCGGATCTGGTTACCACTAAACC-3′; reverse primer *tpcn1*-w/oSC-R, 5′-ACCGGTccGCCTCCGGAGTTAAT-GCTGTTTGTGGC-3′. The two additional bases included to ensure in-frame fusion are indicated in lowercase. PCR was performed using the

Phusion® High-Fidelity DNA polymerase (NEB, MA, USA) using the same settings described above except that the 20 sec annealing step was at 67°C and the extension step was for 2 min at 72°C. After the final elongation step at 72°C for 8 min, the amplicons were analyzed and purified as described above.

The results of these reactions were two amplicons as follows: (1) a G-GECO1.2 fragment and (2) a linearized TPC1 vector, which were annealed in a Gibson assembly reaction using the Gibson Assembly® master mix (New England Biolabs Inc.). The results were confirmed by Sanger Sequencing. mRNA encoding TPC1–G-GECO1.2 or TPC1[L264P]–G-GECO1.2 was synthesized using the mMESSAGE mMACHINE SP6 transcription kit as described above, and ~150 pg of the mRNA was injected into the blastodisc of AB wild-type embryos at the one-cell stage.

Preparation of primary cell cultures

Primary cultured SMCs used for immunolabeling were prepared and fixed via well-established methods (Kelu et al., 2015, 2017). To prepare primary cultured SMCs for live-cell imaging, several minor modifications were made to this protocol following recommendations reported by Sassen et al. (2017). Importantly, the cells were incubated in L-15 medium (Gibco Life Technologies, MA, USA) containing 10% fetal bovine serum (Gibco Life Technologies); 1× glutamine (Invitrogen Corp., Eugene, OR, USA); and 1.2% penicillin-streptomycin (10,000 units/ml; Gibco Life Technologies) for all the steps leading up to plating, and a plating time of 20 min was used. In addition, for experiments in which the nuclei were to be labeled, cells were resuspended in culture medium containing 1 µg/ml Hoechst 33258 (Molecular Probes, Thermo Fisher Scientific, Inc.) prior to plating.

Preparation and live imaging of cells expressing TPC1–G-GECO1.2

Cells expressing TPC1–G-GECO1.2 (TPC1-GG) were plated for ~45 min, as described above, and washed three times with Ca^{2+}-free solution comprising 145 mM NaCl, 5 mM KCl, 3 mM $MgCl_2$, 10 mM glucose, 1 mM EGTA and 20 mM HEPES (pH 7.4). Cells were then maintained in 2 ml of this solution for the start of image acquisition. Halfway through imaging (i.e. ~2 min into the 4 min time-lapse series), 500 µl of a solution containing 10 µM ionomycin (Sigma-Aldrich, Merck Group, MI, USA) and 50 mM $CaCl_2$ was added to the cells, to provide final concentrations of 2 µM and 10 mM, respectively. The ionomycin and $CaCl_2$ step was used to permeabilize the cells and saturate any of the remaining TPC1-GG that was not already fluorescing. In some experiments, TPC1-GG cells were treated with 25 µM BAPTA-AM [1,2-Bis(2-aminophenoxy)ethane-N,N,N′, N′-tetraacetic acid tetrakis(acetoxymethyl ester); Thermo Fisher Scientific, Inc.] or 25 µM dimethyl-BAPTA-AM (Thermo Fisher Scientific) for 45 min at ~28°C during plating in the presence of 0.03% w/v Pluronic F127 (Sigma-Aldrich), followed by a 15 min de-esterification. In another series of experiments TPC1-GG cells were treated with 10 µM trans-Ned-19 (Enzo Life Sciences, Inc., NY, USA) for 45 min at ~28°C during plating. All experiments were carried out within 45 min to 2 h after plating, and the temperature was maintained at ~28°C throughout imaging. Images were acquired as described below.

Quantification of TPC1-decorated vesicle dynamics

Time-lapse image files were imported into ImageJ (https://imagej.nih.gov/ij/; National Institutes of Health, MD, USA) and analyzed with the TrackMate plugin (Tinevez et al., 2017). Images were split into separate channels and subjected to the 'smoothened' function once, before proceeding with particle tracking of the labeled puncta. The Laplacian of Gaussian (LoG) segmentation detector feature of the plugin was selected, and an estimated particle diameter of 0.5 µm and a threshold of 0.5 were used. The median filter of the plugin was disabled, and subpixel localization was enabled. Thresholding of the particles resolved by the LoG detector was performed using the 'Quality' values, such that those that formed the first histogram peak with low quality values were removed. The remaining particles were analyzed using the Linear Assignment Problem (LAP) tracker, with a linking maximum distance of 0.5 µm; gap closing distance of 0.5 µm over 2

frames; and with track splitting and merging enabled. The velocities of the individual TPC1 puncta were taken as a close approximation only, as we did not take into consideration any displacements that might have occurred within the z-plane. A value of 0.2 µm/s was selected as a threshold value to exclude background noise during data analysis.

Quantification of β-dystroglycan puncta in whole-mount immunolabeled embryos

To quantify observed differences in β-dystroglycan labeling patterns between controls, *tpcn1* morphants, E8 crispants and bafilomycin A1-treated embryos, the percentage area of β-dystroglycan labeling within a region of interest (ROI) of 23 µm×23 µm was calculated. This value was obtained from confocal images of the ROI, which were acquired of the dorsal region of somite 8 and processed using ImageJ as follows: confocal z-stacks of β-dystroglycan fluorescence images were maximally projected, after which they were subjected to the 'smoothened' and 'threshold' functions in the default settings. The 'analyze particles' function was then used to calculate the total percentage area of β-dystroglycan within the ROI.

Quantification of TPC1–G-GECO1.2 fluorescence

To quantify the number of TPC1-GG-recorded Ca^{2+} events at the ends of isolated SMCs, a ROI spanning one-fifth of the entire length of each SMC was used. The TrackMate plugin of ImageJ was used to quantify the number of TPC1-GG puncta within this ROI before the addition of ionomycin and $CaCl_2$, as well as the number of TPC1-GG puncta in the entire cell both before and after the addition of ionomycin and $CaCl_2$. A filter was set to exclude puncta with 'quality values' <3. To produce traces of all the TPC1-GG puncta over time against percentage maximal GG fluorescence, TPC1-GG puncta in the entire SMC were tracked using the LoG detector of the TrackMate plugin, as described above. A table containing 'spot statistics' was exported to Microsoft Office Professional Plus Excel 2013 (Microsoft Corp., WA, USA), and values for 'Mean intensity', 'Track ID' and 'frame' were subsequently exported to Minitab 17.3.1 (Minitab Inc., State College, PA, USA) for graph plotting.

Pharmacological treatment of primary cell cultures with nocodazole

A stock solution of nocodazole (Abcam, Cambridge, UK) was prepared at 5 µM in DMSO and stored at −20°C. In one series of live-cell imaging experiments, primary cultured cells were imaged for ~2 min in culture medium on a heated stage (at ~28°C). Nocodazole was then added to the cells to a final concentration of 1 µM. Image acquisition was halted, but the imaging chamber was kept on the heated stage for ~15 min, after which, the same cell was imaged for a further ~2 min. The TrackMate plugin of ImageJ was used to quantify the dynamics of TPC1–EGFP puncta before and after treatment with nocodazole, as described above. Values for velocity were extracted from the 'spot statistics' function for each time-lapse series and exported to Minitab 17.3.1 for graph plotting.

Pharmacological treatment of whole embryos

Stock solutions of bafilomycin A1 (1 mM; Tocris Bioscience, Bristol, UK) and trans-Ned-19 were prepared as previously described (Kelu et al., 2015). As both compounds are membrane permeable (Yoshimori et al., 1991; Naylor et al., 2009), dechorionated AB wild-type embryos were incubated at ~28°C with 1 µM bafilomycin A1 or 100 µM trans-Ned-19 (both diluted in Danieau's solution) using methods described previously (Kelu et al., 2015).

Whole-mount immunohistochemistry and immunocytochemistry

Embryos at ~24 hpf were dechorionated (as described above) and fixed with phosphate-buffered saline (PBS) containing 4% paraformaldehyde overnight at 4°C. After fixation, excess paraformaldehyde was removed and the embryos were washed first with PBS and then with PBS containing 0.1% Triton X-100 (PBST), after which they were permeabilized with PBST containing 1% DMSO (PBSTD) for 1 h. Permeabilized embryos were then incubated with blocking buffer (PBST containing 10% goat serum and 1% bovine serum albumin; Sigma-Aldrich) for 2 h, after which they were further incubated with blocking buffer containing F59 mouse anti-myosin

heavy chain (used at 1:20; F59 Developmental Studies Hybridoma Bank, IA, USA) or anti-β-dystroglycan (used at 1:50; 43DAG1/8D5 Leica Biosystems, Wetzlar, Germany) at ~4°C overnight. To label embryos with anti-TPC1 (used at 1:25; A15847 ABclonal, MA, USA), slight modifications were made such that 0.2% Triton X-100 was used in place of 0.1% Triton X-100, and the antibody incubation time was increased to 2 days. After the primary antibody incubation step, embryos were then washed extensively before being incubated with an Alexa Fluor 488-conjugated goat anti-rabbit IgG (H+L) antibody or Alexa Fluor 488-conjugated goat anti-mouse IgG (H+L) antibody (both used at 1:200 and both from Molecular Probes) at ~4°C overnight in the dark. The embryos were then incubated with Alexa Fluor 568–phalloidin (used at 1:50; Molecular Probes) and 1 µg/ml Hoechst 33258 (Thermo Fisher Scientific, Inc.) at room temperature for 1 h in the dark to label F-actin and the nuclei, respectively. The embryos were washed extensively with wash buffer (a 1:10 dilution of blocking buffer) between each incubation step. At the end of these final wash steps, the labeled embryos were rinsed with PBST and then with PBS. To improve the incubation and washing efficiencies, gentle shaking was applied throughout using a mini gyro-rocker (Techne SSM3, Cole-Parmer, Stone, UK). Working dilutions of the antibodies and phalloidin were prepared in blocking buffer followed by centrifugation at 16,873 g for 5 min to pellet any unwanted debris.

Colocalization studies and correlation analysis of TPC1 with subcellular markers in primary cultured SMCs

AB wild-type embryos were sequentially injected into the blastodisc at the one-cell stage with ~150 pg *tpcn1–EGFP* or *tpcn1–tdTomato* mRNA and ~50 pg *actc1b-mKate2–rab5c*, *–rab11ba*, *–rab32b* or *–lamp1* DNA (Addgene, plasmid numbers 109651, 109596, 109622 and 109507, respectively; Hall et al., 2020). At ~48 hpf, muscle cell cultures were prepared as described above. Two reporter channels, one for TPC1–EGFP and one for the appropriate intracellular endolysosomal marker (or TPC1–tdTomato as a positive control), were used for analysis. Pearson's correlation analysis was performed using the ImageJ plugin JaCoP (Bolte and Cordelières, 2006) on single optical sections. To label the SR, AB wild-type embryos were injected sequentially with ~150 pg *tpcn1–EGFP* and ~50 pg *actc1b-mKate2–KDEL* DNA (Addgene, plasmid number 109494) (Hall et al., 2020) at the one-cell stage and muscle cell cultures were prepared and imaged as described above. To label the microtubules, AB embryos were injected with ~150 pg *tpcn1–tdTomato* mRNA, and then the cells were stained with Tubulin Tracker Green (Thermo Fisher Scientific, Inc.) for 45 min at ~28°C during plating in the presence of 0.03% w/v Pluronic F127.

Fluorescent labeling of whole embryos

To co-label cell membranes and the acidic organelles in intact AB wild-type embryos, embryos at ~75% epiboly (~8 hpf) were incubated overnight in Danieau's solution (Westerfield, 2000) containing 25 µM BODIPY® FL C5-ceramide (Thermo Fisher Scientific, Inc.). They were then bathed in Danieau's solution containing 10 µM LysoTracker® Red DND-99 (Thermo Fisher Scientific, Inc.) for 45 min at ~28°C prior to imaging via confocal microscopy at ~24 hpf.

LysoTracker fluorescence was quantified by analyzing confocal *z*-stacks taken through the SMCs in the dorsal region of somite 8. The LysoTracker fluorescence channel was maximally projected, after which a threshold of default settings was applied, and the puncta were quantified using the 'analyze particles' function of ImageJ with the following parameters: size=10–400 pixel^2 and circularity=0.00–1.00. To quantify the organization of LysoTracker-stained organelles at the MJ, the BODIPY® FL C5-Ceramide fluorescence channel was used to define the location of the MJ, and then the 'polygon select tool' was used to draw a rhombus with a base of 20 µm centered on either side of it. This rhombus was used to create an ROI that was overlaid onto the corresponding LysoTracker fluorescence images. The organization of the puncta within this region was quantified by calculating the ratio of the number of particles within the ROI (which comprised two somite boundaries within the confocal image, i.e. somites 7 to 8, and somites 8 to 9), and the total number of puncta in the image.

Confocal imaging of fluorescently labeled embryos and primary cultured cells

Fixed embryos and primary cultured cells were imaged using a TCS SP8 laser scanning confocal microscope (Leica Microsystems GmbH, Wetzlar, Germany) with HC PL APO 40×/1.30 and HC PL APO 60×/1.40 oil objective lenses, respectively. Regarding the embryos, unless otherwise stated, the trunk was imaged from a lateral view at (and posterior to) somite 7. The respective wavelengths (excitation/detection) of the various fluorophores used are as follows: Alexa Fluor 488, 488 nm/519 nm; Alexa Fluor 568, 568 nm/600 nm; GFP, 488 nm/509 nm; tdTomato, 554 nm/581 nm; mKate2, 588 nm/635 nm; LysoTracker® Red DND-99, 576 nm/590 nm; and DAPI and Hoechst 33258, 350 nm/461 nm. The temperature was maintained at ~28°C for all live (cell and embryo) imaging experiments using a heated imaging chamber (TOKAI HIT Stage Top Incubator®, Shizuoka-ken, Japan). Live embryos were anesthetized by immersion in Danieau's solution containing ~0.02% MS-222 ~5 min before the start of imaging. For time-lapse imaging of whole embryos and cultured cells, single confocal images were acquired at 867 ms and 655 ms intervals, respectively. For other experiments, images were acquired as a confocal *z*-stack by sequential scanning between the different channels to minimize fluorescence crosstalk. In some experiments, single optical sections alone were used for data analysis, whereas in others they were reconstructed using ImageJ.

Super-resolution imaging of primary cultured cells

Live imaging of primary cultured cells was also performed using a Zeiss LSM 980 with Airyscan 2 in conjunction with a 561 nm DPSS laser and Airyscan GaAsP detector. Images were acquired using a 63×/1.4 oil objective lens and the ZEN3.1 software (Zeiss, Germany).

Fluorescence imaging of TPC1–EGFP-expressing embryos

To assess TPC1–EGFP fluorescence with or without injection of the *tpcn1*-T-MO, AB wild-type embryos at ~2.5 hpf were manually dechorionated as described above and placed in individual wells in a 96-well flat bottom cell culture plate (SPL Life Sciences, Gyeonggi, South Korea). Bright-field and EGFP fluorescence images were acquired using exposure times of 4 ms and 1.5 s, respectively, using a Nikon Digital Sight DS-5Mc digital camera mounted on a Nikon AZ100 microscope (Nikon Instruments Inc., Melville, NY, USA) with a Nikon AZ Plan Apo 5×/0.5 NA objective lens. EGFP fluorescence was observed with a Nikon Intensilight C-HGFI mercury light source and the GFP/FITC single band filter cube, using excitation wavelengths of 465–495 nm and emission wavelengths ≥515 nm. All images were acquired using the NIS-Elements Advanced Research software (Nikon Instruments Inc.).

Statistical analysis and figure preparation

All image measurements were carried out using ImageJ. Numerical data were exported to Microsoft Office Professional Plus Excel 2013 (Microsoft Corp., WA, USA) for basic descriptive statistics and to GraphPad Prism (GraphPad Software, San Diego, CA, USA) for graph plotting. Note, in the box plots in Fig. 4Ae, the line in the middle indicates the mean and not the median. Data were also imported into Minitab 17.3.1 to run one-way ANOVA and calculate significance with Tukey's multiple-comparison test or Fisher's least significant difference (LSD) test. Figures were prepared using CorelDRAW version X8 (Corel Corp., Ottawa, ON, Canada).

Peer review history

The peer review history is available online at https://journals.biologists.com/jcs/article-lookup/doi/10.1242/jcs.259564.

References

Arpağ, G., Shastry, S., Handcock, W. O. and Tüzel, E. (2014). Transport by populations of slow and fast kinesins uncovers novel family-dependent motor characteristics important for *in vivo* function. *Biophys. J.* **107**, 1896-1904. doi:10.1016/j.bpj.2014.09.009

Basset, D. I., Bryson-Richardson, R. J., Daggett, D. F., Gautier, P., Keenan, D. G. and Currie, P. D. (2003). Dystrophin is required for the formation of stable muscle attachments in the zebrafish embryo. *Development* **130**, 5851-5860. doi:10.1242/dev.00799

Berridge, M. J., Bootman, M. D. and Roderick, H. L. (2003). Calcium signaling dynamics, homeostasis and remodeling. *Nat. Rev. Mol. Cell Biol.* **4**, 517-529. doi:10.1038/nrm1155

Blagden, C. S., Currie, P. D., Ingham, P. W. and Hughes, S. M. (1997). Notochord induction of zebrafish slow muscle mediated by sonic hedgehog. *Genes Dev.* **11**, 2163-2175. doi:10.1101/gad.11.17.2163

Bolte, S. and Cordelières, F. P. (2006). A guided tour into subcellular colocalization analysis in light microscopy. *J. Microsc.* **224**, 153-174. doi:10.1111/j.1365-2818.2006.01706.x

Brailoiu, E., Churamani, D., Cai, X., Schrlau, M. G., Brailoiu, G. C., Gao, X., Hooper, R., Boulware, M. J., Dun, N. J., Marchant, J. S. et al. (2009). Essential requirement for two-pore channel 1 in NAADP-mediated calcium signaling. *J. Cell Biol.* **186**, 201-209. doi:10.1083/jcb.200904073

Brennan, C., Mangoli, M., Dyer, C. E. F. and Ashworth, R. (2005). Acetylcholine and calcium signalling regulates muscle fibre formation in the zebrafish embryo. *J. Cell Sci.* **118**, 5181-5190. doi:10.1242/jcs.02625

Calcraft, P. J., Ruas, M., Pan, Z., Cheng, X., Arredouani, A., Hao, X., Tang, J., Rietdorf, K., Teboul, L., Chuang, K.-T. et al. (2009). NAADP mobilizes calcium from acidic organelles through two-pore channels. *Nature* **459**, 596-601. doi:10.1038/nature08030

Castonguay, J., Orth, J. H. C., Müller, T., Sleman, F., Grimm, C., Wahl-Schott, C., Biel, M., Mallmann, R. T., Bildl, W., Schulte, U. et al. (2017). The two-pore channel TPC1 is required for efficient protein processing during early and recycling endosomes. *Sci. Rep.* **7**, 10038. doi:10.1038/s41598-017-10607-4

Charvet, B., Malbouyres, M., Pagnon-Minot, A., Ruggiero, F. and Le Guellec, D. (2011). Development of the zebrafish myoseptum with emphasis on the myotendinous junction. *Cell Tissue Res.* **346**, 439-449. doi:10.1007/s00441-011-1266-7

Chaumet, A., Wright, G. D., Seer, S. H., Tham, K. M., Gunko, N. V. and Bard, F. (2015). Nuclear envelope-associated endosomes deliver surface proteins to the nucleus. *Nat. Commun.* **6**, 8218. doi:10.1038/ncomms9218

Cheng, X., Zhang, X., Gao, Q., Samie, M. A., Azar, M., Tsang, W. L., Dong, L., Sahoo, N., Li, X., Zhuo, Y. et al. (2014). The intracellular Ca^{2+} channel MCOLN1 is required for sarcolemma repair to prevent muscular dystrophy. *Nat. Med.* **20**, 1187-1192. doi:10.1038/nm.3611

Cheung, C.Y., Webb, S. E., Meng, A. and Miller, A. L. (2006). Transient expression of apoaequorin in zebrafish embryos: extending the ability to image calcium transients during later stages of development. *Int. J. Dev. Biol.* **50**, 561-569. doi:10.1387/ijdb.062151cc

Cheung, C. Y., Webb, S. E., Love, D. R. and Miller, A. L. (2011). Visualization, characterization and modulation of Ca^{2+} signaling during the development of slow muscle cells in intact zebrafish embryos. *Int. J. Dev. Biol.* **55**, 153-174. doi:10.1387/ijdb.103160cc

Churamani, D., Hooper, R., Rahman, T., Brailoiu, E. and Patel, S. (2013). The N-terminal region of two-pore channel 1 regulates trafficking and activation by NAADP. *Biochem. J.* **453**, 147-151. doi:10.1042/BJ20130474

Cong, L., Ran, F. A., Cox, D., Lin, S., Barretto, R., Habib, N., Hsu, P. D., Wu, X., Jiang, W., Marraffini, L. A. et al. (2013). Multiplex genome engineering using CRISPR/Cas systems. *Science* **339**, 819-823. doi:10.1126/science.1231143

Cortés, F., Daggett, D., Bryson-Richardson, R. J., Neyt, C., Maule, J., Gautier, P., Hollway, G. E., Keenan, D. and Currie, P. D. (2003). Cadherin-mediated differential cell adhesion controls slow muscle cell migration in the developing zebrafish myotome. *Dev. Cell* **5**, 865-876. doi:10.1016/S1534-5807(03)00362-9

Cremer, T., Neefjes, J. and Berlin, I. (2020). The journey of Ca^{2+} through the cell – pulsing through the network of ER membrane contact sites. *J. Cell Sci.* **133**, jcs249136. doi:10.1242/jcs.249136

Davis, L. C., Morgan, A. J. and Galione, A. (2020). NAADP-regulated two-pore channels drive phagocytosis through endo-lysosomal Ca^{2+} nanodomains, calcineurin and dynamin. *EMBO J.* **39**, e104058. doi:10.15252/embj.2019104058

De Araujo, M. E. G., Liebscher, G., Hess, M. W. and Huber, L. A. (2020). Lysosomal size matters. *Traffic* **21**, 60175. doi:10.1111/tra.12714

Devoto, S. H., Melançon, E., Eisen, J. S. and Westerfield, M. (1996). Identification of separate slow and fast muscle precursor cells *in vivo*, prior to somite formation. *Development* **122**, 3371-3380. doi:10.1242/dev.122.11.3371

Diaz-Hernandez, M., Cox, J. A., Migita, K., Haines, W., Egan, T. M. and Voigt, M. M. (2002). Cloning and characterization of two novel zebrafish P2X receptor subunits. *Biochim. Biophys. Res. Commun.* **295**, 849-853. doi:10.1016/S0006-291X(02)00760-X

Dong, X.-P., Shen, D., Wang, X., Dawson, T., Li, X., Zhang, Q., Cheng, X., Zhang, Y., Weisman, L. S., Delling, M. et al. (2010). PI(3,5)P$_2$ controls membrane trafficking by direct activation of mucolipin Ca^{2+} release channels in the endolysosome. *Nat. Commun.* **1**, 38. doi:10.38/ncomms1037

Dowling, J. J., Gibbs, E. M. and Feldman, E. L. (2008). Membrane traffic and muscle: Lessons from human disease. *Traffic* **9**, 1035-1043. doi:10.1111/j.1600-0854.2008.00716.x

Dwight, Z. L., Palais, R. and Wittwer, C. T. (2012). uAnalyze: Web-based high-resolution DNA melting analysis with comparison to thermodynamic predictions. *IEEE/ACM Trans. Comput. Biol. Bioinform.* **9**, 1805-1811. doi:10.1109/TCBB.2012.112

Eden, E. R., Sanchez-Heras, E., Tsapara, A., Sobota, A., Levine, T. P. and Futter, C. E. (2016). Annexin A1 tethers membrane contact sites that mediate ER to endosome cholesterol transport. *Dev. Cell* **37**, 473-483. doi:10.1016/j.devcel.2016.05.005

Eisen, J. S. and Smith, J. C. (2008). Controlling morpholino experiments: Don't stop making antisense. *Development* **135**, 1735. doi:10.1242/dev.001115

El-Brolosy, M. A. and Stainier, D. Y. R. (2017). Genetic compensation: a phenomenon in search of mechanisms. *PLoS Genet.* **13**, e1006780. doi:10.1371/journal.pgen.1006780

Ervasti, J. M. and Campbell, K. P. (1993). A role for the dystrophin-glycoprotein complex as a transmembrane linker between laminin and actin. *J. Cell Biol.* **122**, 809-823. doi:10.1083/jcb.122.4.809

Galione, A. (2019). NAADP receptors. *Cold Spring Harb. Perspect. Biol.* **11**, a035071. doi:10.1101/cshperspect.a035071

Gembella, S. and Vogel, F. (2002). Spatial arrangement of white muscle fibers and myoseptal tendons in fishes. *Comp. Biochem. Physiol.* **133**, 1013-1037. doi:10.1016/S1095-6433(02)00186-1

Goody, M. F., Kelly, M. W., Reynolds, C. J., Khalil, A., Crawford, B. D. and Henry, C. A. (2012). NAD+ biosynthesis ameliorates a zebrafish model of muscular dystrophy. *PLoS Biol.* **10**, e1001409. doi:10.1371/journal.pbiol.1001409

Goody, M. F., Carter, E. V., Kilroy, E. H., Mavis, L. and Henry, C. A. (2017). "Muscling" throughout life: Integrating studies of muscle development, homeostasis, and disease in zebrafish. *Curr. Top. Dev. Biol.* **124**, 197-234. doi:10.1016/bs.ctdb.2016.11.002

Granger, E., McNee, G., Allan, V. and Woodman, P. (2014). The role of the cytoskeleton and molecular motors in endosomal dynamics. *Semin. Cell Dev. Biol.* **31**, 20-29. doi:10.1016/j.semcdb.2014.04.011

Grimm, C., Chen, C.-C., Wahl-Schott, C. and Biel, M. (2017). Two-pore channels: Catalyzers of endolysosomal transport and function. *Front. Pharmacol.* **8**, 45. doi:10.3389/fphar.2017.00045

Guo, C., Webb, S. E., Chan, C. M. and Miller, A. L. (2020). TPC2-mediated Ca^{2+} signaling is required for axon extension in caudal primary motor neurons in zebrafish embryos. *J. Cell Sci.* **133**, jcs244780. doi:10.1242/jcs.244780

Gupta, V., Kawahara, G., Gundry, S. R., Chen, A. T., Lencer, W. I., Zhou, Y., Zon, L. I., Kunkel, L. M. and Beggs, A. H. (2011). The zebrafish *dag1* mutant: a novel genetic model for dystroglycanopathies. *Hum. Mol. Genet.* **20**, 1712-1725. doi:10.1093/hmg/ddr047

Guyon, J. R., Mosley, A. N., Zhou, Y., O'Brien, K. F., Sheng, X., Chiang, K., Davidson, A. J., Volinski, J. M., Zon, L. I. and Kunkel, L. M. (2003). The dystrophin associated protein complex in zebrafish. *Hum. Mol. Genet.* **12**, 601-615. doi:10.1093/hmg/ddg071

Hall, T. E., Martel, N., Ariotti, N., Xiong, Z., Lo, H. P., Ferguson, C., Rae, J., Lim, Y.-W. and Parton, R. G. (2020). *In vivo* cell biological screening identifies an endocytic capture mechanism for T-tubule formation. *Nat. Commun.* **11**, 3711. doi:10.1038/s41467-020-17486-w

Henry, C. A., Hall, L. A., Hille, M. B., Solnica-Krezel, L. and Cooper, M. S. (2000). Somites in zebrafish doubly mutant for *knypek* and *trilobite* form without internal mesenchymal cells or compaction. *Curr. Biol.* **10**, 1063-1066. doi:10.1016/S0960-9822(00)00677-1

Henry, C. A., McNulty, I. M., Durst, W. A., Munchel, S. E. and Amacher, S. L. (2005). Interactions between muscle fibers and segment boundaries in zebrafish. *Dev. Biol.* **287**, 346-360. doi:10.1016/j.ydbio.2005.08.049

Hill, J. T., Demarest, B. L., Bisgrove, B. W., Su, Y. C., Smith, M. and Yost, H. J. (2014). Poly peak parser: Method and software for identification of unknown indels using sanger sequencing of polymerase chain reaction products. *Dev. Dyn.* **243**, 1632-1636. doi:10.1002/dvdy.24183

Horton, J. S., Wakamp, C. T., Speck, M. and Stokes, A. J. (2015). Two-pore channel 1 interacts with citron kinase, regulating completion of cytokinesis. *Channels* **9**, 21-29. doi:10.4161/19336950.2014.978676

Hu, Y., Xie, S. and Yao, J. (2016). Identification of novel reference genes suitable for qRT-PCR normalization with respect to the zebrafish developmental stage. *PLoS ONE* 11, e0149277. doi:10.1371/journal.pone.0149277

Huang, P., Zou, Y., Zhong, X. Z., Cao, Q., Zhao, K., Zhu, M. X., Murrell-Lagnado, R. and Dong, X.-P. (2014). P2X4 forms functional ATP-sensitive cation channels on lysosome membranes regulated by luminal pH. *J. Biol. Chem.* 289, 17658-17667. doi:10.1074/jbc.M114.552158

Huang, X., Jiang, C., Yu, L. and Yang, A. (2020). Current and emerging approaches for studying inter-organelle membrane contact sites. *Front. Cell Dev. Biol.* 8, 195. doi:10.3389/fcell.2020.00195

Jackson, H. E. and Ingham, P. W. (2013). Control of muscle fibre-type diversity during embryonic development: The zebrafish paradigm. *Mech. Dev.* 130, 447-457. doi:10.1016/j.mod.2013.06.001

Jao, L.-E., Wente, S. R. and Chen, W. (2013). Efficient multiplex biallelic zebrafish genome editing using a CRISPR nuclease system. *Proc. Natl. Acad. Sci. USA* 110, 13904-13909. doi:10.1073/pnas.1308335110

Jin, X., Zhang, Y., Alharbi, A., Habashi, A., Alhoshani, A. and Parrington, J. (2020). Targeting two-pore channels: Current progress and future challenges. *Trends Pharmacol. Sci.* 41, 582-594. doi:10.1016/j.tips.2020.06.002

Jung, J.-J., Inamdar, S. M., Tiwari, A. and Choudhury, A. (2012). Regulation of intracellular membrane trafficking and cell dynamics by syntaxin-6. *Biosci. Rep.* 32, 383-391. doi:10.1042/BSR20120006

Kaisto, T., Rahkila, P., Marjomäki, V., Parton, R. G. and Metsikkö, K. (1999). Endocytosis in skeletal muscle fibers. *Exp. Cell Res.* 253, 551-560. doi:10.1006/excr.1999.4659

Kelu, J. J., Chan, H. L. H., Webb, S. E., Cheng, A. H. H., Ruas, M., Parrington, J., Galione, A. and Miller, A. L. (2015). Two-pore channel 2 activity is required for slow muscle cell-generated Ca^{2+} signaling during myogenesis in intact zebrafish. *Int. J. Dev. Biol.* 59, 313-325. doi:10.1387/ijdb.150206am

Kelu, J. J., Webb, S. E., Parrington, J., Galione, A. and Miller, A. L. (2017). Ca^{2+} release via two-pore channel type 2 (TPC2) is required for slow muscle cell myofibrillogenesis and myotomal patterning in intact zebrafish embryos. *Dev. Biol.* 425, 109-129. doi:10.1016/j.ydbio.2017.03.031

Kelu, J. J., Webb, S. E., Galione, A. and Miller, A. L. (2019). Characterization of ADP-ribose cyclase 1-like (ARC1-like) activity and NAADP signaling during slow muscle development in zebrafish embryos. *Dev. Biol.* 445, 211-225. doi:10.1016/j.ydbio.2018.11.005

Kilpatrick, B. S., Eden, E. R., Schapira, A. H., Futter, C. E. and Patel, S. (2013). Direct mobilisation of lysosomal Ca^{2+} triggers complex Ca^{2+} signals. *J. Cell Sci.* 126, 60-66. doi:10.1242/jcs.118836

Kilpatrick, B. S., Eden, E. R., Hockey, L. N., Yates, E., Futter, C. E. and Patel, S. (2017). An endosomal NAADP-sensitive two-pore Ca^{2+} channel regulates ER-endosome membrane contact sites to control growth factor signaling. *Cell. Rep.* 18, 1636-1645. doi:10.1016/j.celrep.2017.01.052

Kimmel, C. B., Ballard, W. W., Kimmel, S. R., Ullmann, B. and Schilling, T. F. (1995). Stages in the embryonic development of zebrafish. *Dev. Dyn.* 203, 253-310. doi:10.1002/aja.1002030302

Kinnear, N. P., Boittin, F.-X., Thomas, J. M., Galione, A. and Evans, A. M. (2004). Lysosome-sarcoplasmic reticulum junctions: a trigger zone for calcium signaling by nicotinic acid adenine dinucleotide phosphate and endothelin-1. *J. Biol. Chem.* 279, 54319-54326. doi:10.1074/jbc.M406132200

Klumperman, J. and Raposo, G. (2014). The complex ultrastucture of the endolysosomal system. *Cold Spring Harb. Perspec. Biol.* 6, a016857. doi:10.1101/cshperspect.a016857

Leung, C. F., Miller, A. L., Korz, V., Chong, S.-W., Sleptsova-Freidrich, I. and Webb, S. E. (2009). Visualization of stochastic Ca^{2+} signals in the formed somites during the early segmentation period in intact normally developing zebrafish embryos. *Dev. Growth. Diff.* 51, 617-637. doi:10.1111/j.1440-169X.2009.01123.x

Li, H., Pei, W., Vergarajauregui, S., Zerfas, P. M., Raben, N., Burgess, S. W. and Puertollano, R. (2017). Novel degenerative and developmental defects in a zebrafish model of mucolipidosis type IV. *Hum. Mol. Genet.* 26, 2710-2718. doi:10.1093/hmg/ddx158

Lin, P.-H., Duann, P., Komazaki, S., Park, K. H., Li, H., Sun, M., Sermersheim, M., Gumpper, K., Parrington, J., Galione, A. et al. (2015). Lysosomal two-pore channel subtype 2 (TPC2) regulates skeletal muscle autophagic signaling. *J. Biol. Chem.* 290, 3377-3389. doi:10.1074/jbc.M114.608471

Lin-Moshier, Y., Keebler, M. V., Hooper, R., Boulware, M. J., Liu, X., Churamani, D., Abood, M. E., Walseth, T. F., Brailoiu, E., Patel, S. et al. (2014). The two-pore channel (TPC) interactome unmasks isoform-specific roles for TPCs in endolysosomal morphology and cell pigmentation. *Proc. Natl. Acad. Sci. USA.* 111, 13087-13092. doi:10.1073/pnas.1407004111

Livak, K. J. and Schmittgen, T. D. (2001). Analysis of relative gene expression data using real-time quantitative PCR and the 2−ΔΔCT method. *Methods* 25, 402-408. doi:10.1006/meth.2001.1262

Marchant, J. S. and Patel, S. (2015). Two-pore channels at the intersection of endolysosomal membrane traffic. *Biochem. Soc. Trans.* 43, 434-441. doi:10.1042/BST20140303

McCurley, A. T. and Callard, G. V. (2008). Characterization of housekeeping genes in zebrafish: Male-female differences and effects of tissue type, developmental stage and chemical treatment. *BMC Mol. Biol.* 9, 102. doi:10.1186/1471-2199-9-102

Meeker, N. D., Hutchinson, S. A., Ho, L. and Trede, N. S. (2007). Method for isolation of PCR-ready genomic DNA from zebrafish tissues. *BioTechniques* 43, 610-614. doi:10.2144/000112619

Moccia, F., Negri, S., Faris, P., Perna, A., De Luca, A., Soda, T., Berra-Romani, R. and Guerra, G. (2021). Targeting the endolysosomal two-pore channels to treat cardiovascular disorders in the novel coronavirus disease 2019. *Front. Physiol.* 12, 629119. doi:10.3389/fphys.2021.629119

Moreno-Layseca, P., Icha, J., Hamidi, H. and Ivaska, J. (2019). Integrin trafficking in cells and tissues. *Nat. Cell Biol.* 21, 122-132. doi:10.1038/s41556-018-0223-z

Morgan, A. J. and Galione, A. (2014). Two-pore channels (TPCs): current controversies. *BioEssays* 36, 173-183. doi:10.1002/bies.201300118

Naganawa, Y. and Hirata, H. (2011). Developmental transition of touch response from slow muscle-mediated coilings to fast muscle-mediated burst swimming in zebrafish. *Dev. Biol.* 355, 194-204. doi:10.1016/j.ydbio.2011.04.027

Naylor, E., Arredouani, A., Vasudevan, S. R., Lewis, A. M., Parkesh, R., Mizote, A., Rosen, D., Thomas, J. M., Izumi, M., Ganesan, A. et al. (2009). Identification of a chemical probe for NAADP by virtual screening. *Nat. Chem. Biol.* 5, 220-226. doi:10.1038/nchembio.150

Ono, Y., Yu, W., Jackson, H. E., Parkin, C. A. and Ingham, P. W. (2015). Adaxial cell migration in the zebrafish embryo is an active cell autonomous property that requires the Prdm1a transcription factor. *Differentiation* 89, 77-86. doi:10.1016/j.diff.2015.03.002

Papadopoulos, J. S. and Agarwala, R. (2007). COBALT: constraint-based alignment tool for multiple protein sequences. *Bioinformatics* 23, 1073-1079. doi:10.1093/bioinformatics/btm076

Parsons, M. J., Campos, I., Hirst, E. M. A. and Stemple, D. L. (2002). Removal of dystroglycan causes severe muscular dystrophy in zebrafish embryos. *Development* 129, 3505-3512. doi:10.1242/dev.129.14.3505

Patel, S. and Kilpatrick, B. S. (2018). Two-pore channels and disease. *Biochim. Biophys. Acta Mol. Cell Res.* 1865, 1678-1686. doi:10.1016/j.bbamcr.2018.05.004

Pethig, R., Kuhn, M., Payne, R., Adler, E., Chen, T.-H. and Jaffe, L. F. (1989). On the dissociation constants of BAPTA-type calcium buffers. *Cell Calcium* 10, 491-498. doi:10.1016/0143-4160(89)90026-2

Raffaello, A., Mammucari, C., Gherardi, G. and Rizzuto, R. (2016). Calcium at the center of cell signaling: Interplay between endoplasmic reticulum, mitochondria, and lysosomes. *Trends. Biochem. Sci.* 41, 1035-1049. doi:10.1016/j.tibs.2016.09.001

Raiborg, C., Wenzel, E. M. and Stenmark, H. (2015). ER-endosome contact sites: molecular compositions and functions. *EMBO J.* 34, 1848-1859. doi:10.15252/embj.201591481

Reddy, A., Caler, E. V. and Andrews, N. W. (2001). Plasma membrane repair is mediated by Ca^{2+}-regulated exocytosis of lysosomes. *Cell* 106: 157-169. doi:10.1016/S0092-8674(01)00421-4

Robu, M. E., Larson, J. D., Nasevicius, A., Beiraghi, S., Brenner, C., Farber, S. A. and Ekker, S. C. (2007). p53 activation by knockdown technologies. *PLoS Genet.* 3, e78. doi:10.1371/journal.pgen.0030078

Rossi, A., Kontarakis, Z., Gerri, C., Nolte, H., Hölper, S., Krüger, M. and Stainier, D. Y. R. (2015). Genetic compensation induced by deleterious mutations but not gene knockdowns. *Nature* 524, 230-233. doi:10.1038/nature14580

Ruas, M., Reitdorf, K., Arredouani, A., Davis, L. C., Lloyd-Evans, E., Koegel, H., Funnell, T. M., Morgan, A. J., Ward, J. A., Watanabe, K. et al. (2010). Purified TPC isoforms form NAADP receptors with distinct roles for Ca^{2+} signaling and endolysosomal trafficking. *Curr. Biol.* 20, 703-709. doi:10.1016/j.cub.2010.02.049

Saint-Amant, L. and Drapeau, P. (1998). Time course of the development of motor behaviors in the zebrafish embryo. *J. Neurobiol.* 37, 622-632. doi:10.1002/(SICI)1097-4695(199812)37:4<622::AID-NEU10>3.0.CO;2-S

Samarut, É., Lissouba, A. and Drapeau, P. (2016). A simplified method for identifying early CRISPR-induced indels in zebrafish embryos using high resolution melting analysis. *BMC Genomics* 17, 547. doi:10.1186/s12864-016-2881-1

Sambrook, J. and Russell, D. W. (2006). Purification of nucleic acids by extraction with phenol:chloroform. *Cold Spring Harb. Prot.* 2006, pdb.prot4455. doi:10.1101/pdb.prot4455

Sassen, W. A., Lehne, F., Russo, G., Wargenau, S., Dübel, S. and Köster, R. W. (2017). Embryonic zebrafish primary cell culture for transfection and live cellular and subcellular imaging. *Dev. Biol.* 430, 18-31. doi:10.1016/j.ydbio.2017.07.014

Shimomura, O. (1997). Membrane permeability of coelenterazine analogues measured with fish eggs. *Biochem. J.* 326, 297-298. doi:10.1042/bj3260297

Speksnijder, J. E., Miller, A. L., Weisenseel, M. H., Chen, T.-H. and Jaffe, L. F. (1989). Calcium buffer injections block fucoid egg development by facilitating calcium diffusion. *Proc. Natl. Acad. Sci. USA* 86, 6607-6611. doi:10.1073/pnas.86.17.6607

Stellabotte, F. and Devoto, S. H. (2007). The teleost dermomyotome. *Dev. Dyn.* 236, 2442-2443. doi:10.1002/dvdy.21253

Tang, R., Dodd, A., Lai, D., McNabb, W. C. and Love, D. R. (2007). Validation of zebrafish (*Danio rerio*) reference genes for quantitative real-time RT-PCR normalization. *Acta Biochim. Biophys. Sin.* **39**, 384-390. doi:10.1111/j.1745-7270.2007.00283.x

Tinevez, J. Y., Perry, N., Schindelin, J., Hoopes, G. M., Reynolds, G. D., Laplantine, E., Bednarek, S. Y., Shorte, S. L. and Eliceiri, K. W. (2017). TrackMate: an open and extensible platform for single-particle tracking. *Methods* **115**, 80-90. doi:10.1016/j.ymeth.2016.09.016

Varshney, G. K., Pei, W., LaFave, M. C., Idol, J., Xu, L., Gallardo, V., Carrington, B., Bishop, K., Jones, M. P., Li, M. et al. (2015). High-throughput gene targeting and phenotyping in zebrafish using CRISPR/Cas9. *Genome Res.* **25**, 1030-1042. doi:10.1101/gr.186379.114

Varshney, G. K., Carrington, B., Pei, W., Bishop, K., Chen, Z., Fan, C., Xu, L., Jones, M., LaFave, M. C., Ledin, J. et al. (2016). A high-throughput functional genomics workflow based on CRISPR/Cas9-mediated targeted mutagenesis in zebrafish. *Nat. Protoc.* **11**, 2357-2375. doi:10.1038/nprot.2016.141

Vassileva, K., Marsh, M. and Patel, S. (2020). Two-pore channels as master regulators of membrane trafficking and endocytic well-being. *Curr. Opin. Physiol.* **17**, 163-168. doi:10.1016/j.cophys.2020.08.002

Verdeny-Vilanova, I., Wehnekamp, F., Mohan, N., Álverez, A. S., Borbely, J. S., Otterstom, J. J., Lamb, D. C. and Lakadamyali, M. (2017). 3D motion of vesicles along microtubules helps them to circumvent obstacles in cells. *J. Cell Sci.* **130**, 1904-1916. doi:10.1242/jcs.201178

Webb, S. E. and Miller, A. L. (2013). Microinjecting holo-aequorin into dechorionated and intact zebrafish embryos. *Cold Spring Harb. Protoc.* **5**, 447-455. doi:10.1101/pdb.prot072967

Westerfield, M. (2000). *The Zebrafish Book. A Guide for the Laboratory use of Zebrafish (Danio rerio)*, 4th edn. Eugene, USA: University of Oregon Press.

Wood, A. J. and Currie, P. D. (2017). Development aspects of zebrafish myotendinous junctions: a model system for understanding muscle basement membrane formation and failure. *Curr. Pathobiol. Rep.* **5**, 197-205. doi:10.1007/s40139-017-0140-z

Yang, J., Zhao, Z., Gu, M., Feng, X. and Xu, H. (2019). Release and uptake mechanisms of vesicular Ca^{2+} stores. *Protein Cell* **10**, 8-19. doi:10.1007/s13238-018-0523-x

Yoshimori, T., Yamamoto, A., Moriyama, Y., Futai, M. and Tashiro, Y. (1991). Bafilomycin A_1, a specific inhibitor of vacuolar-type H^+-ATPase, inhibits acidification and protein degradation in lysosomes of cultured cells. *J. Biol. Chem.* **266**, 17707-17712. doi:10.1016/S0021-9258(19)47429-2

Zajac, A. L., Goldman, Y. E., Holzbaur, E. L. F. and Ostap, E. M. (2013). Local cytoskeletal and organelle interactions impact molecular-motor-driven early endosomal trafficking. *Curr. Biol.* **23**, 1173-1180. doi:10.1016/j.cub.2013.05.015

Zhao, Y., Araki, S., Wu, J., Teramoto, T., Chang, Y.-F., Nakano, M., Abdelfattah, A. S., Fujiwara, M., Ishihara, T., Nagai, T. et al. (2011). An expanded palette of genetically encoded Ca^{2+} indicators. *Science* **333**, 1888-1891. doi:10.1126/science.1208592

Zhu, M. X., Ma, J., Parrington, J., Calcraft, P. J., Galione, A. and Evans, A. M. (2010a). Calcium signaling via two-pore channels: local or global, that is the question. *Am. J. Physiol. Cell Physiol.* **298**, C430-C441. doi:10.1152/ajpcell.00475.2009

Zhu, M. X., Evans, A. M., Ma, J., Parrington, J. and Galione, A. (2010b). Two-pore channels for integrative Ca^{2+} signaling. *Commun. Integr. Biol.* **3**, 12-17. doi:10.4161/cib.3.1.9793
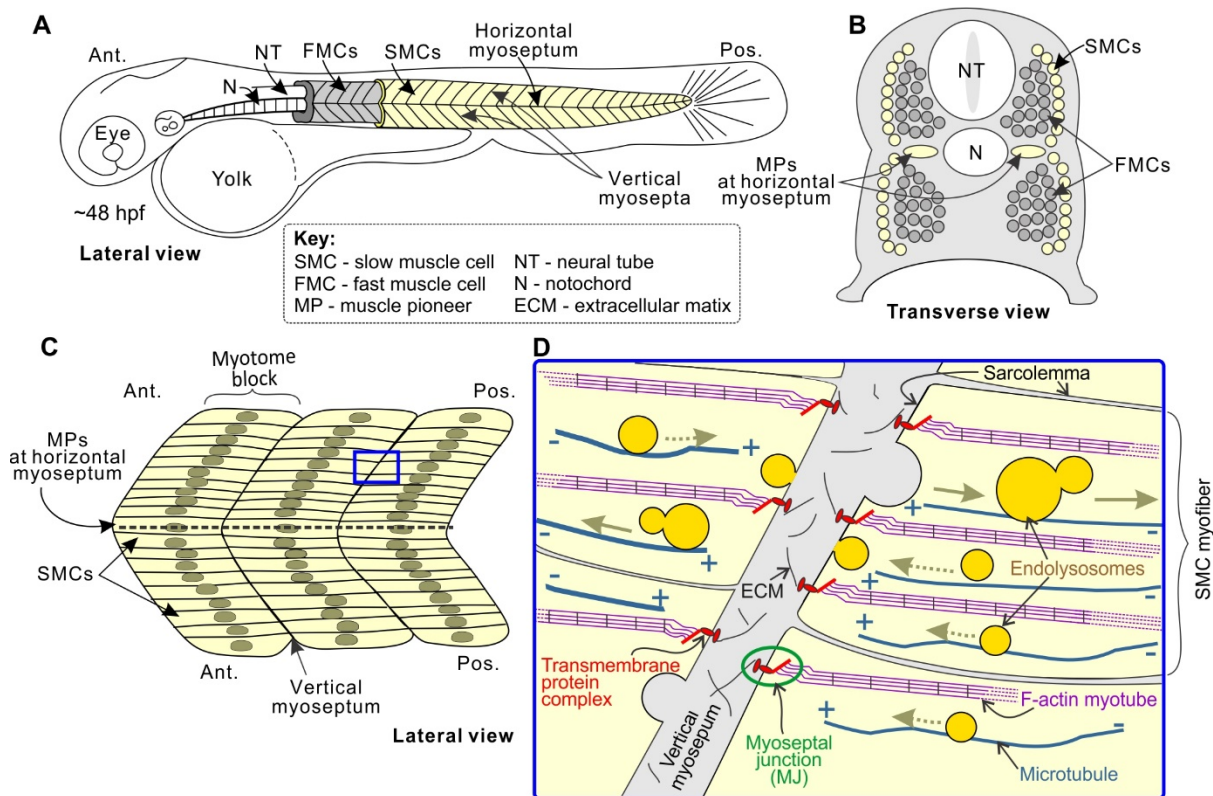
Fig. S1. Schematics to show the location of the slow muscle cells (SMCs) in the trunk of zebrafish embryos at ~24 hpf. **(A)** Lateral view of the entire embryo showing the superficial distribution of the SMCs in relation to the more deeply located fast muscle cells (FMCs). The neural tube (NT), notochord (N), and both the horizontal and vertical myosepta are also shown. **(B)** Transverse view of the trunk at ~24 hpf showing the location of the SMCs, FMCs, NT, N, and muscle pioneers (MPs) at the horizontal myoseptum. **(C)** Lateral view of the SMCs at higher magnification. The region bounded by the blue rectangle is shown in greater detail in **(D)**. **(D)** Schematic to show relevant components of the myoseptal junctions (MJs). These include the lateral end of the F-actin-rich myotubes, which are linked to extracellular matrix (ECM) components in the vertical myoseptal via the terminal sarcomeric z-lines, cortical actin cytoskeleton, and transmembrane protein complexes. Microtubules (with their plus and minus ends) and endolysosomes are also shown. Ant. and Pos. are anterior and posterior, respectively. Not drawn to scale.
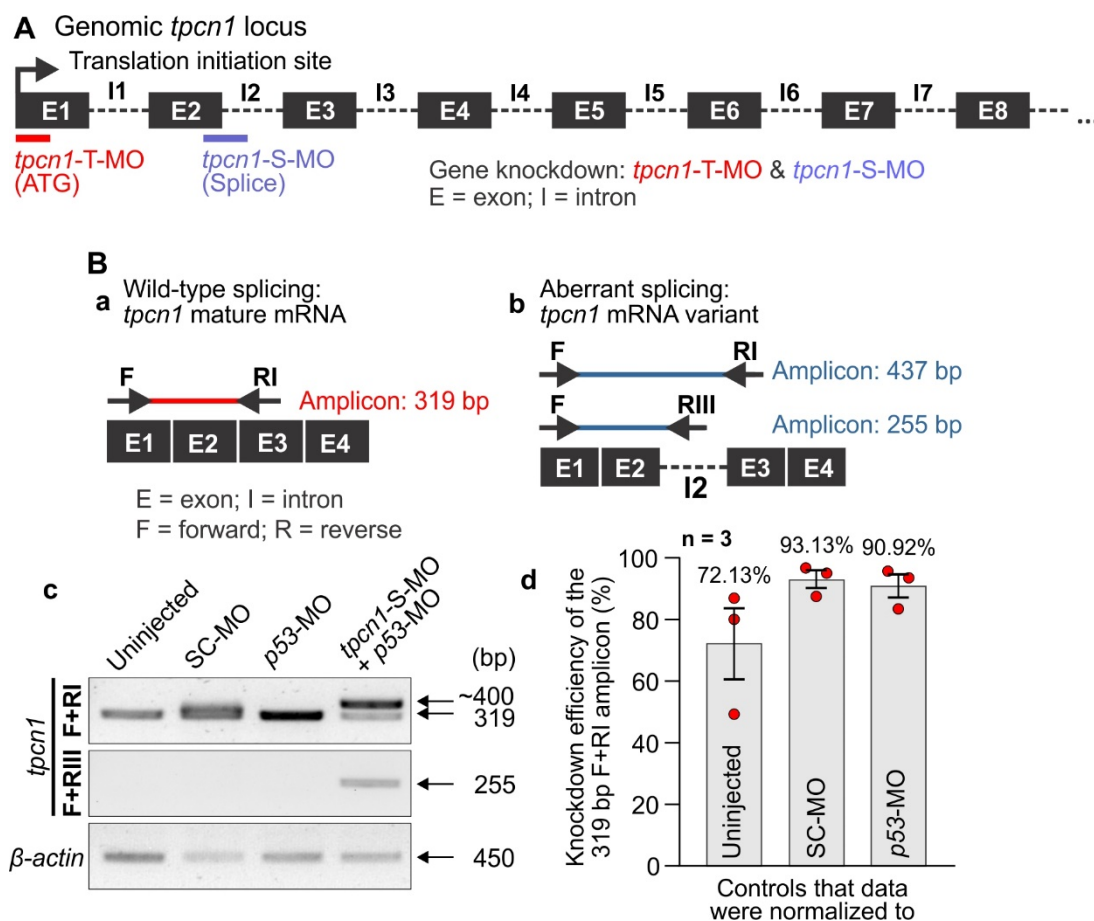
Fig. S2. Design and evaluation of two independent MOs that target the *tpcn1* transcripts in zebrafish. (A) A translation-blocking *tpcn1*-MO (*tpcn1*-T-MO) was designed to bind to a region spanning the start codon of the principal *tpcn1* splice variant in zebrafish (*tpcn1-202*; Ensembl transcript ID: ENSDART00000138123.4), and the splice-blocking *tpcn1*-MO (*tpcn1*-S-MO) bound to an exon-intron junction common to all three *tpcn1* transcripts (*tpcn1-201*: ENSDART00000090102.6; *tpcn1-202*; *tpcn1-203:* ENSDART00000187745.1). **(Ba)** Schematic of the wild-type *tpcn1* mRNA transcript (with exons 1-4 alone) showing the design of one forward (F) and one reverse (RI) primer for performing reverse-transcription PCR (RT-PCR). **(Bb)** A possible aberrant *tpcn1* mRNA transcript containing intron 2, which might result from the splice-blocking action of the *tpcn1*-S-MO (again only exons 1-4 are shown). The design of another reverse primer (RIII) to detect intron-inclusion is also shown. **(Bc,Bd)** RT-PCR analyses of *tpcn1* transcripts following *tpcn1*-S-MO-mediated knockdown resulted in aberrant mRNA splicing, which was characterized as intron inclusion. **(Bc)** A representative 2% agarose gel showing the RT-PCR products after the F+RI and F+RIII primer sets were used to amplify different portions of the *tpcn1* mRNA transcript. *β-actin* was used as the internal control. **(Bd)** Bar chart to show the mean ± SEM knockdown efficiency of the *tpcn1*-S-MO, which was evaluated from agarose gels, such as the one shown in **(Bc)**. When normalized to the *p53*-MO controls, the knockdown efficiency of normal *tpcn1* transcripts in *tpcn1*-S-MO- + *p53*-MO-injected embryos was ~90.9%.
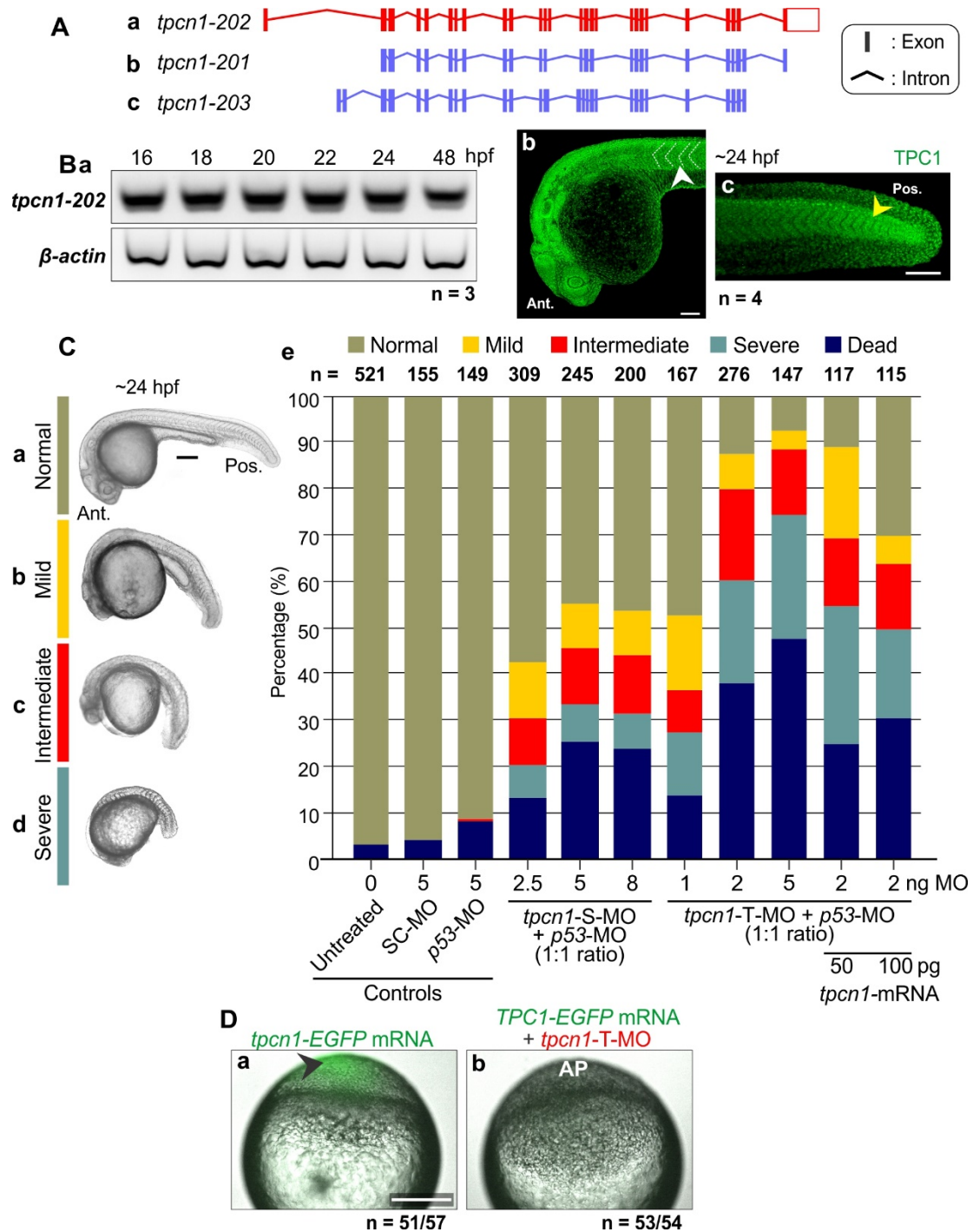
Fig. S3. The *tpcn1* variants in zebrafish, expression of *tpcn1-202* mRNA and TPC1 protein in embryos, dose-dependent effect of the *tpcn1*-MOs (with/without mRNA rescue) on zebrafish development at ~24 hpf and effect of the *tpcn1*-T-MO on the expression of TPC1-EGFP. (A) Schematics of the three transcript variants of *tpcn1* in zebrafish, with the principal isoform (*tpcn1-202*) shown in red. **(Ba)** Representative cDNA gel to show the expression of *tpcn1-202* mRNA in embryos from 16 hpf to 48 hpf. At each time point, RNA was extracted from excised trunks and subjected to RT-PCR. The *β-actin* house-keeping gene was used as a loading control. These data show

that the *tpcn1-202* transcript is expressed in embryos at ~16 hpf (during the segmentation period) when the somites are forming. However, evidence on a publicly available transcriptomic database (Expression Atlas; https://www.ebi.ac.uk/gxa/home) indicates that *tpcn1* (ensdarg00000062362) is expressed as early as the zygote and cleavage stages in zebrafish. **(Bb,Bc)** Expression of TPC1 at ~24 hpf (i.e., ~30 somite stage) in **(Bb)** mature anterior somites (white arrowhead), and **(Bc)** immature forming somites in the tail (yellow arrowhead). **(C)** Injection of the different *tpcn1*-MOs (or the *tpcn1*-T-MO plus *tpcn1-202* mRNA) at the 1-cell stage generated a range of different phenotypes by ~24 hpf. Representative examples of these phenotypes are shown in the bright-field images **(Ca-Cd)**. Embryos were defined as: **(Ca)** being grossly normal; having **(Cb)** mild, **(Cc)** intermediate or **(Cd)** severe deformities; or dead. **(Ce)** Stacked bar graph showing the percentage of embryos that exhibited a particular phenotype at ~24 hpf. The embryos were either untreated or else they were injected at the 1-cell stage with: 5 ng standard control- (SC-) MO; 5 ng *p53*-MO; *tpcn1*-S-MO + *p53*-MO at a 1:1 ratio from 2.5 ng – 8 ng; *tpcn1*-T-MO + *p53*-MO at a 1:1 ratio from 1 ng -5 ng; or 2 ng *tpcn1*-T-MO + 2 ng *p53*-MO plus 50 pg or 100 pg *tpcn1-202* mRNA. Both the *tpcn1*-T-MO and *tpcn1*-S-MO produced a dose-dependent response with regards to the numbers of embryos exhibiting differing amounts of phenotypic disruption or death. When one-cell stage embryos were injected into the yolk with the *tpcn1*-T-MO and into the blastodisc with a *tpcn1* 'rescue' mRNA construct, there was a partial rescue of the MO-induced phenotype. In **(B)** and **(C)**, ant. and pos, are anterior and posterior, respectively. **(D)** Representative examples of embryos injected with *in vitro* synthesized mRNA encoding enhanced green fluorescent protein (EGFP) tagged to the C-terminus of TPC1 (*tpcn1-EGFP* mRNA) either **(Da)** alone or **(Db)** with the *tpcn1*-T-MO. These are EGFP (green) fluorescence images superimposed on the corresponding bright-field images of shield stage (~6 hpf) embryos. In the presence of *tpcn1*-T-MO, the number of embryos with observable fluorescence (i.e., to ~1.85%), when compared with embryos injected with *tpcn1-EGFP* alone (i.e., ~89.5%). EGFP fluorescence is indicated by black arrowhead and AP is animal pole. The images are representative of 3 biological replicates each containing ~15 embryos per treatment condition. Scale bars, 100 μm **(Bb,Bc)** and 200 μm **(C,D)**.
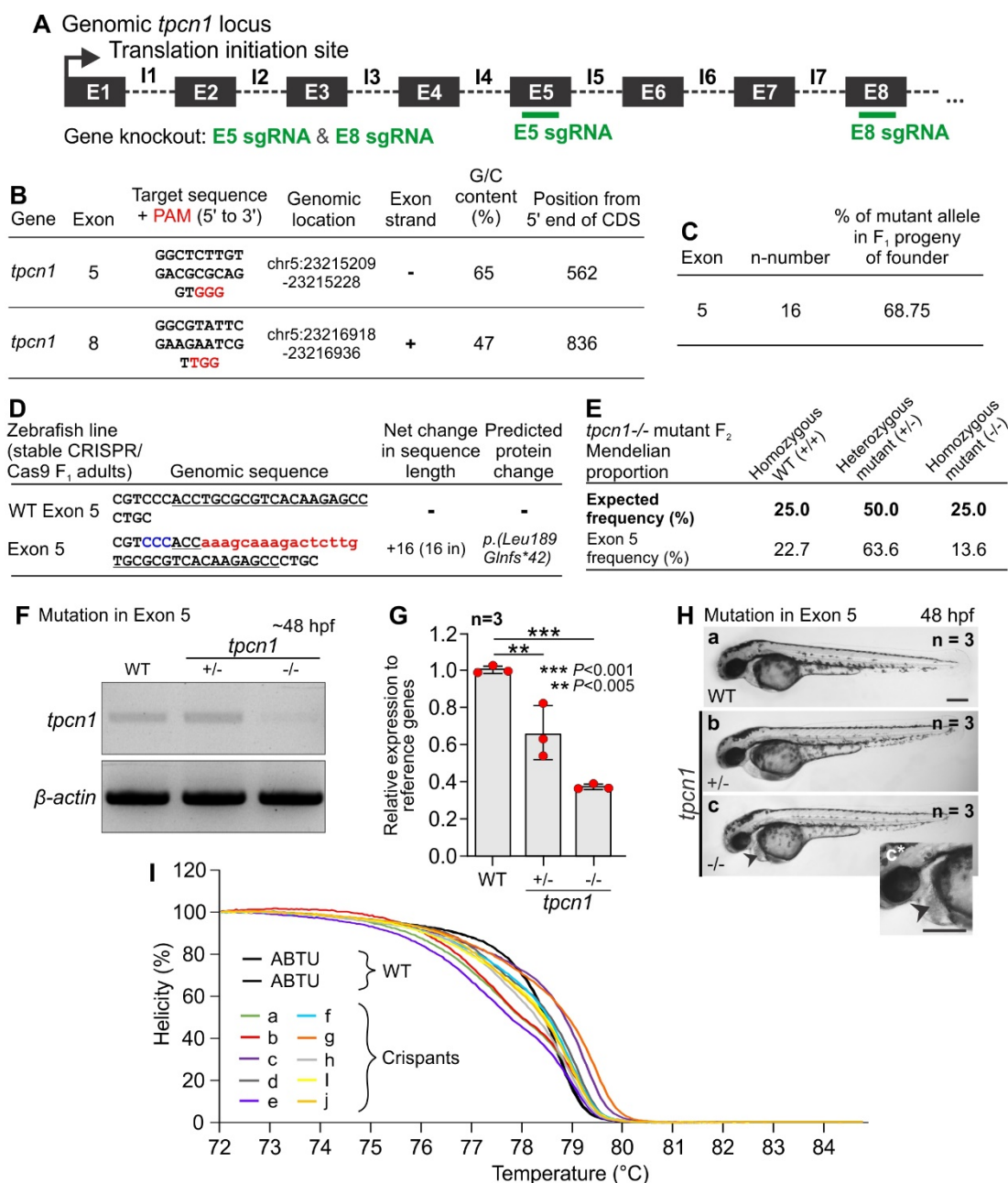
Fig. S4. Design and evaluation of gene knockdown by CRISPR/Cas9. Two single guide RNAs (sgRNAs) were selected that had the lowest number of predicted off-target sites that would target regions common to all three *tpcn1* transcript variants in zebrafish. **(A)** The genomic locus of zebrafish *tpcn1*, showing exons (E) 1-8, introns (I) 1-7, and the location of the E5 and E8 sgRNAs. **(B)** Table to show the *tpcn1* sgRNA target (PAM) sequence (in red) and information about the genomic location, exon number, strand orientation, G/C content and position from the 5' end of the coding region. **(C,D)** Of the embryos injected with exon 5 sgRNA + *Cas9* mRNA and raised to adulthood, several stable F_1 heterozygotes with indels in *tpcn1* were identified from which a single line containing a 16-base pair (bp) insertion was bred to homozygosity. **(C)** Table showing the percentage of mutant alleles identified in the F_1 progeny after outcrossing the F_0 *tpcn1* mosaic line to ABTU wild-type fish. **(D)** Indel mutation

identified within the CRISPR/Cas9 target site in a stable F_1 clutch generated by outcrossing F_0 *tpcn1* mosaic fish to the ABTU wild-type line. In the wild-type sequence of exon 5, the target site is underlined. In the mutant sequence, insertions (in) are represented by lower case red letters. The net change in length is given and the predicted protein change is described using standard nomenclature. **(E)** Frequency of homozygous wild-type (WT; +/+), heterozygous *tpcn1* mutant (+/-) and homozygous *tpcn1* mutant (-/-) zebrafish from a *tpcn1*+/- incross (n=32 fish from 3 clutches). **(F,G)** This line possessed a frameshift mutation, which was predicted to express a truncated form of the TPC1 protein less than half the length of the wild-type protein (i.e., 231 amino acids (aa) out of 805 aa in the principal TPC1 protein isoform). It was therefore expected to be missing the highly conserved activation and ion-conducting regions crucial to TPC1 function. RT-PCR and qRT-PCR of *tpcn1* mRNA in *tpcn1* homozygotes revealed a significant reduction relative to wild-type, suggesting nonsense-mediated decay (Conti and Izaurralde, 2005) **(F)** RT-PCR gel comparing the level of *tpcn1* transcript between the ABTU wild-type, *tpcn1-/+* and *tpcn1-/-* embryos. *β-actin* was used as the loading control. **(G)** mRNA expression levels of *tpcn1* determined by qRT-PCR (relative to *actb2, mob4, lsm12b* and *elfa*) in ~48-hpf ABTU wild-type, *tpcn1+/-* and *tpcn1-/-* embryos (n=3 clutches; performed in triplicate). The data are presented as mean ± SEM (as well as individual data points), and were compared using one-way ANOVA and Tukey's multiple-comparison test. **(H)** Representative bright-field extended depth-of-field images showing examples of ABTU wild-type, *tpcn1-/+* and *tpcn1-/-* embryos at ~48 hpf. The black arrowheads in **(Hc)** and **(Hc*)** indicate the accumulation of blood cells in the heart of the *tpcn1* mutants. Otherwise, the mutants were mostly comparable to ABTU wild-type embryos at ~48 hpf. We found that ~40% of the heterozygous embryos could be grown to adulthood for breeding purposes. Scale bar, 1 mm. **(I)** To generate *tpcn1* crispants, wild-type embryos were injected with the *tpcn1* exon 8 sgRNA + *Cas9* mRNA. These embryos were individually genotyped using high resolution melt analysis (HRMA) after phenotypic analysis was performed on immunolabelled embryos. The shift in melting curves amplified from individually genotyped ~48 hpf *tpcn1* crispant embryos compared to wild-type embryos, was used as an indicator that the *tpcn1* exon 8 sgRNA was effective in generating Cas9-mediated indels at its *tpcn1* target sequence. This HRMA line graph shows the *tpcn1* crispants (n = 10) and ABTU-wildtypes (n = 2).
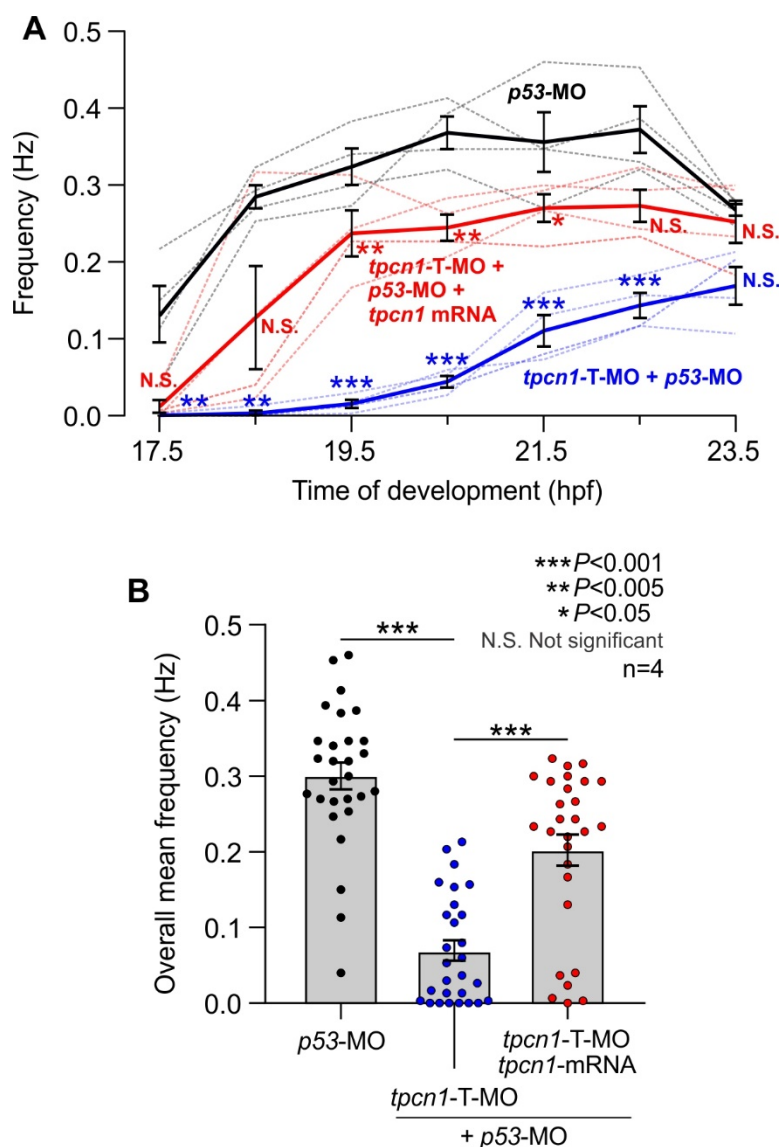
Fig. S5. Effect of MO-based knockdown on the spontaneous coiling behaviour of embryos from ~17.5 hpf to ~23.5 hpf. **(A)** Line graph to show the spontaneous coiling frequency (calculated at 1-h intervals between ~17.5 hpf and ~23.5 hpf) of embryos that were injected with: *p53*-MO; *tpcn1*-T-MO + *p53*-MO; or *tpcn1*-MO + *p53*-MO + *tpcn1* mRNA (n=4 for each). The mean ± SEM spontaneous coiling frequency (solid lines) and the data from individual experiments (dashed lines) observed during the first 5 min at each time point. **(B)** Bar graph (with individual value points) to show the overall mean ± SEM spontaneous coiling frequency from ~17.5 hpf to ~23.5 hpf across the different treatment groups. In both graphs the *tpcn1*-T-MO + *p53*-MO data were compared statistically with the *p53*-MO data, whereas the *tpcn1*-MO + *p53*-MO + *tpcn1* mRNA data were compared with the *tpcn1*-T-MO + *p53*-MO data. Spontaneous coiling behaviour was chosen for comparison because it results mainly from excitation-contraction of SMCs (Naganawa and Hirata, 2011; Hirata et al., 2012).
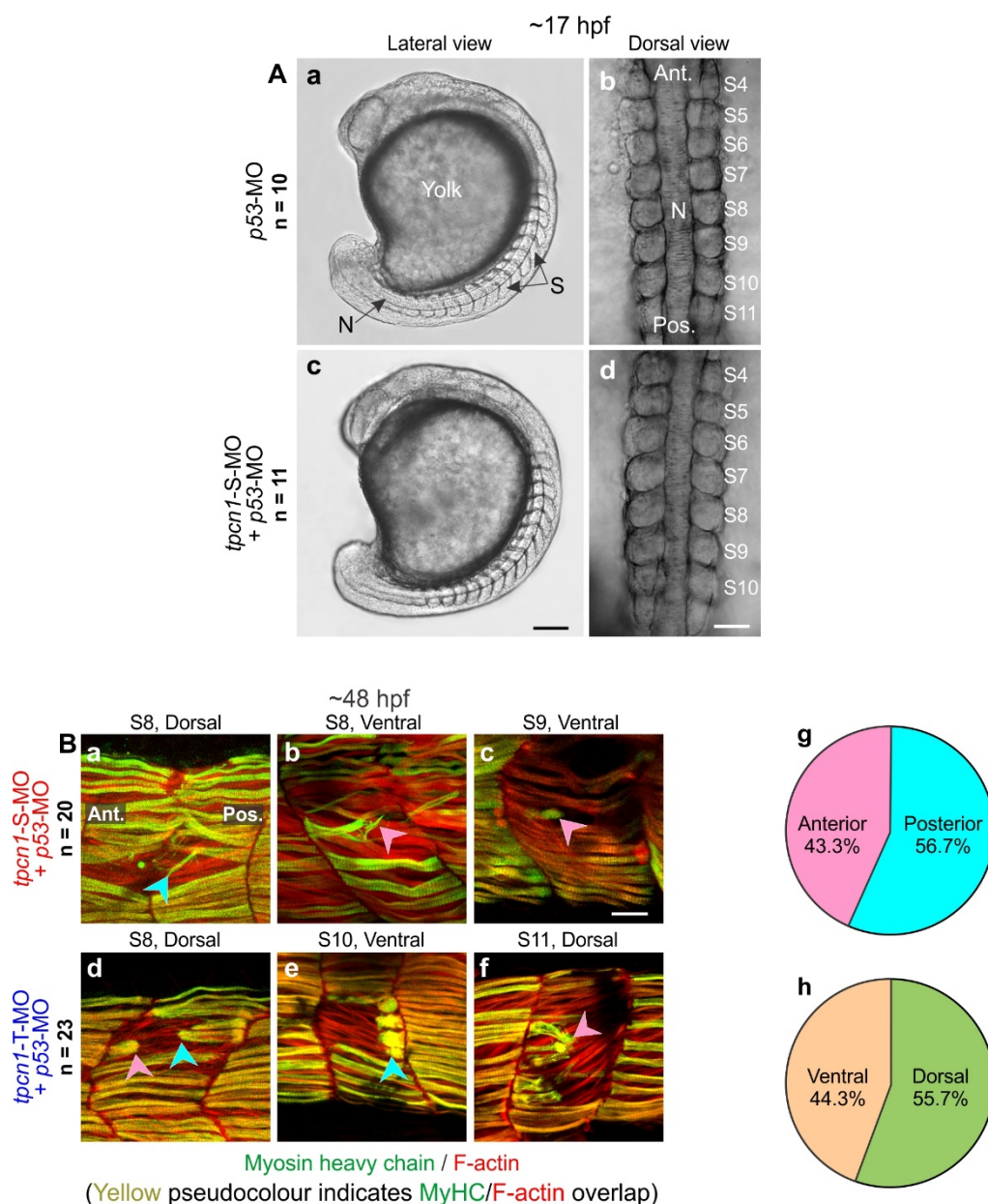
Fig. S6. Effect of MO-based knockdown of TPC1 on somite formation at ~17 hpf and the location of SMC detachments at ~48 hpf. (A) Embryos were injected at the 1-cell stage with **(Aa,Ab)** *p53*-MO or **(Ac,Ad)** *tpcn1-S-MO + p53*-MO, and bright-field images were acquired from the **(Aa,Ac)** lateral and **(Ab,Ad)** dorsal views at ~17 hpf. **(B)** Embryos were injected at the 1-cell stage with **(Ba-Bc)** *tpcn1-S-MO + p53*-MO or **(Bd-Bf)** *tpcn1*-T-MO + *p53*-MO. They were fixed at ~48 hpf and then immunolabeled with an antibody to myosin heavy chain (green) and co-labelled with fluorescent phalloidin to reveal the localisation of F-actin (red). S8-S11 indicate somites 8-11, respectively. The pink and blue arrowheads indicate SMCs detached on the anterior and posterior ends of the myotome boundaries, respectively. **(Bg,Bh)** Pie charts to show the proportion of detachments that occurred from the **(Bg)** anterior or posterior, and **(Bh)** ventral or dorsal regions of somites. Ant. and Pos. are anterior and posterior, respectively. Scale bars, 200 µm **(Ac)**, 50 µm **(Ad)**, and 20 µm **(B)**.
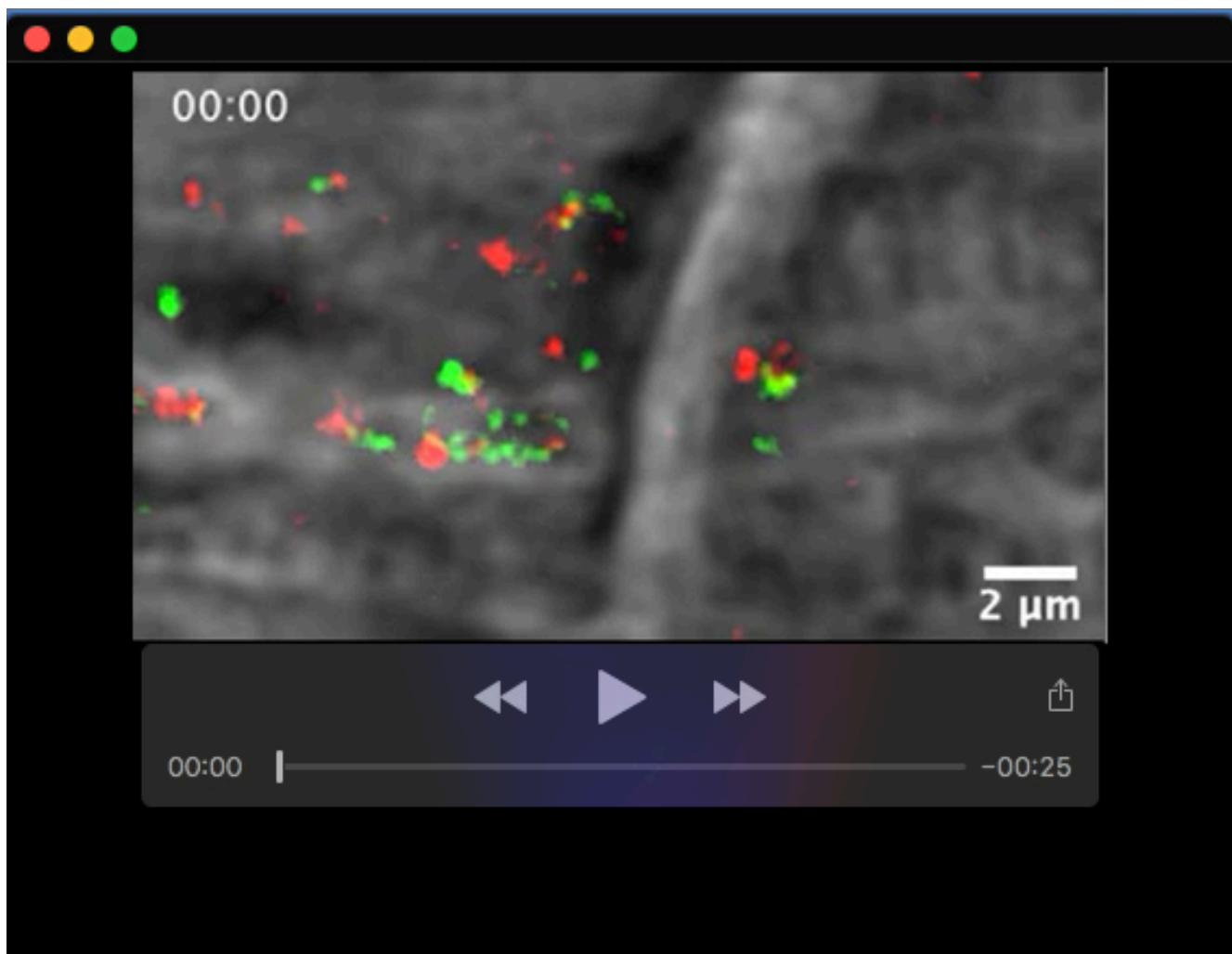
Movie 1. Time-series showing TPC1-decorated vesicles moving in an anterograde direction towards the MJ (pink arrow), and in a retrograde direction from the MJ (blue arrow) in the SMCs of an intact ~24 hpf embryo.
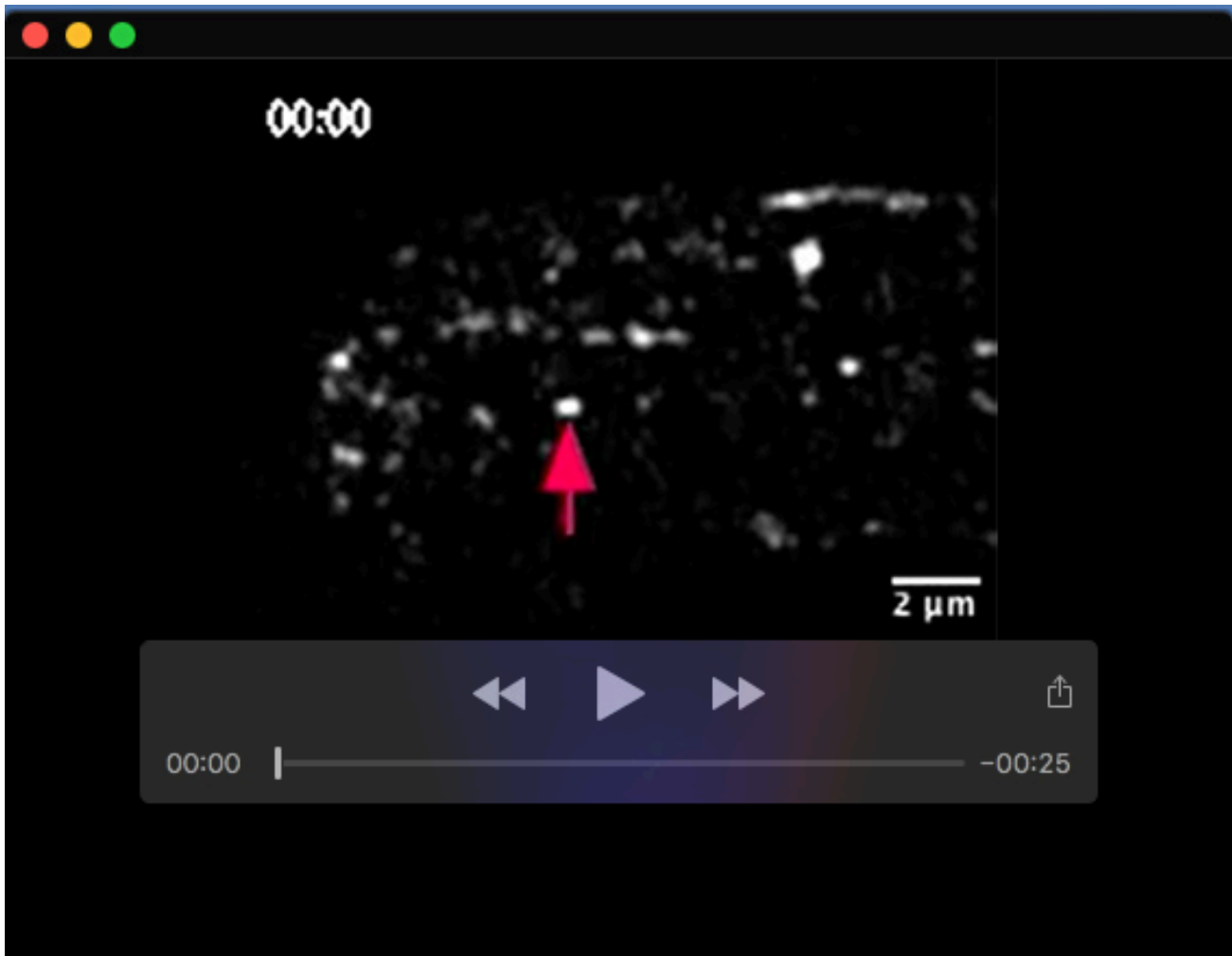
Movie 2. Time-series showing a TPC1-decorated vesicle (see pink arrow) moving in an anterograde direction towards the MJ at the end of a primary cultured SMC.

References

Conti, E. and Izaurralde, E. (2005). Nonsense-mediated mRNA decay: Molecular insights and mechanistic variations across species. *Curr. Op. Cell Biol*. **17**, 316-325. doi:S0955-0674(05)00047-5

Hirata, H., Wen, H., Kawakami, Y., Naganawa, Y., Ogino, K., Yamada, K., Saint-Amant, L., Low, S.E., Cui, W.W., Zhou, W., Sprague, S.M., Asakawa, K., Muto, A., Kawakami, K. and Kuwada, J.Y. (2012). Connexin 39.9 protein is necessary for coordinated activation of slow-twitch muscle and normal behaviour in zebrafish. *J. Biol. Chem.* **287**, 19080-1089. doi:10.1074/jbc.M111.308205.

Naganawa, Y. and Hirata, H. (2011). Developmental transition of touch response from slow muscle-mediated coilings to fast muscle-mediated burst swimming in zebrafish. *Dev. Biol.* **355**, 194-204. doi: 10.1016/j.ydbio.2011.04.027